Highly potent anti-SARS-CoV-2 multivalent DARPin therapeutic candidates

Marcel Walser[1,*], Sylvia Rothenberger[2,3,*], Daniel L. Hurdiss[4,5,*], Anja Schlegel[1], Valérie Calabro[1], Simon Fontaine[1], Denis Villemagne[1], Maria Paladino[1], Tanja Hospodarsch[1], Alexandra Neculcea[1], Andreas Cornelius[1], Patricia Schildknecht[1], Mirela Matzner[1], Martin Hänggi[1], Marco Franchini[1], Yvonne Kaufmann[1], Doris Schaible[1], Iris Schlegel[1], Chloe Iss[1], Thamar Looser[1], Susanne Mangold[1], Christel Herzog[1], Dieter Schiegg[1], Christian Reichen[1], Filip Radom[1], Andreas Bosshart[1], Andreas Lehmann[1], Micha A. Haeuptle[1], Alexander Zürcher[1], Toni Vagt[1], Gabriel Sigrist[1], Marcel Straumann [1], Karl Proba[1], Niina Veitonmäki[1], Keith M. Dawson[1], Christof Zitt[1], Jennifer Mayor[2,3], Sarah Ryter[2], Heyrhyoung Lyoo[4], Chunyan Wang[4], Wentao Li[4], Ieva Drulyte[6], Wenjuan Du[4], H. Kaspar Binz[7], Leon de Waal[8], Koert J. Stittelaar[8*], Sarah Taplin[9], Seth Lewis[1], Daniel Steiner[1], Frank J.M. van Kuppeveld[4], Olivier Engler[2,*], Berend-Jan Bosch[4,*], Michael T. Stumpp[1,10,*], Patrick Amstutz [1,*]

*These authors contributed equally to this work

[1]Molecular Partners AG, Wagistrasse 14, 8952 Zurich-Schlieren, Switzerland

[2]Spiez Laboratory, Austrasse, 3700 Spiez, Switzerland

[3]Institute of Microbiology, University Hospital Center and University of Lausanne, Rue du Bugnon 48, 1011 Lausanne, Switzerland

[4]Department Biomolecular Health Sciences, Division Infectious Diseases & Immunology - Virology section, Faculty of Veterinary Medicine, Utrecht University, 3584 CL, Utrecht, The Netherlands.

[5]Cryo-Electron Microscopy, Bijvoet Center for Biomolecular Research, Department of Chemistry, Faculty of Science, Utrecht University, Padualaan 8, 3584 CH Utrecht, The Netherlands

[6]Materials and Structural Analysis, Thermo Fisher Scientific, Eindhoven, 5651 GG, The Netherlands.

[7]Binz Biotech Consulting, Lüssirainstrasse 52, 6300 Zug

[8]Viroclinics Xplore, Landerd Campus, Nistelrooise Baan 3, 5374 RE, Schaijk, The Netherlands; [8*] Wageningen Bioveterinary Research, PO Box 65, 8200 AB, Lelystad, the Netherlands

[9]Integrated Biologix GmbH, Steinenvorstadt, 33, Basel, CH-4051, Switzerland.

[10]To whom correspondence should be addressed:

Michael T. Stumpp; +41 44 755 77 00; info@molecularpartners.com

Summarizing 125-character sentence: **Generation of ensovibep, the first clinical-stage trivalent anti-SARS-CoV-2 therapeutic candidate.**

Keywords: SARS-CoV-2, COVID-19, corona virus, antiviral therapy, post-exposure prophylaxis, DARPin® drug, ankyrin repeat protein, multispecific, ribosome display, ensovibep, MP0420

DARPin® is a registered trademark owned by Molecular Partners AG

Abstract

Globally accessible therapeutics against SARS-CoV-2 are urgently needed. Here, we report the generation of the first anti-SARS-CoV-2 DARPin molecules with therapeutic potential as well as rapid large-scale production capabilities. Highly potent multivalent DARPin molecules with low picomolar virus neutralization efficacies were generated by molecular linkage of three different monovalent DARPin molecules. These multivalent DARPin molecules target various domains of the SARS-CoV-2 spike protein, thereby limiting possible viral escape. Cryo-EM analysis of individual monovalent DARPin molecules provided structural explanations for the mode of action. Analysis of the protective efficacy of one multivalent DARPin molecule in a hamster SARS-CoV-2 infection model demonstrated a significant reduction of pathogenesis. Taken together, the multivalent DARPin molecules reported here, one of which has entered clinical studies, constitute promising therapeutics against the COVID-19 pandemic.

48 **Introduction**

49 Fighting the COVID-19 pandemic will require coordinated global efforts to maximize the benefits of
50 vaccinations and therapeutics(*1*). Even though vaccine and therapeutic development efforts have
51 progressed considerably, there is, and will be, a remaining medical need for globally accessible
52 therapeutics to treat patients and to protect health care workers, as well as individuals with underlying
53 medical conditions that preclude them from being vaccinated. Neutralizing monoclonal antibodies are
54 expected to be critically important and could be readily available(*2-4*), however they are complex to
55 manufacture and come at a considerable cost. These logistical hurdles may severely limit accessibility,
56 thus preventing an effective global solution(*5*).

57

58 DARPin molecules are an emerging class of novel therapeutics that are actively being developed in
59 ophthalmology and oncology, with four molecules at a clinical stage(*6, 7*). Here, we report the
60 generation and characterization of the first anti-viral DARPin molecules in the context of the COVID-
61 19 pandemic. DARPin molecules are based on naturally occurring ankyrin repeat motifs. To generate
62 therapeutic DARPin molecules, a pure *in vitro* approach (i.e. selections via ribosome display) is possible
63 and can be carried out in a very short time frame, only requiring the target protein, in this case the
64 SARS-CoV-2 spike protein or subdomains thereof. Hence, therapeutic DARPin molecules can be
65 prepared independently of patient samples or animal immunizations. DARPin molecules can be
66 monovalent and thus monospecific or linked by peptide linkers to form single-chain multivalent or
67 multispecific DARPin molecules with several specificities. Notably, DARPin molecules can be
68 manufactured by microbial fermentation, and thus be potentially available world-wide within a short
69 time due to lower technical requirements to provide large-scale clinical grade material. Additionally,
70 the high heat stability of DARPin molecules offers the prospect of a reduced cold chain for distribution
71 around the globe.

72

73 The SARS-CoV-2 spike protein(*8, 9*), presented as a metastable prefusion trimer at the viral surface,
74 mediates virus entry into the host cell. The spike protein comprises multiple functional domains: S1,
75 which includes the N-terminal domain (NTD) and the receptor binding domain (RBD) responsible for
76 interaction with the angiotensin-converting enzyme 2 (ACE2) host receptor(*1, 8, 10, 11*), and the S2
77 domain, which is responsible for virus-host cell membrane fusion via extensive, irreversible
78 conformational changes(*12-14*). This domain composition opens the possibility to target several sites
79 on a single viral protein, leading to multiple mechanisms of inhibition. Such a multi-pronged approach
80 is expected to lead to higher potencies, lower doses, and better protection against potential viral
81 escape mutations.

82

83 Here, we present a novel approach using DARPin molecules to simultaneously bind three sites on the
84 trimeric SARS-CoV-2 spike protein. The results reported below describe the development and
85 characterization of monospecific DARPin molecules against distinct domains of the spike protein, the
86 selection process for the most potent monospecific DARPin molecules and, supported by cryo-EM
87 data, their rational combination into highly potent multivalent as well as multispecific DARPin
88 molecules. Furthermore, we demonstrate the protective efficacy of a multivalent DARPin molecule
89 against virus replication and severe disease in a hamster model of COVID-19. We anticipate that
90 antiviral multivalent DARPin molecules have the potential to become an easy-to-deploy antiviral
91 approach for treatment and/or prevention of COVID-19. Based on the results presented here, MP0420
92 or ensovibep - a multispecific RBD-binding DARPin candidate, is currently being studied in Phase 2
93 clinical trials.

Results

Selection and characterization of monovalent DARPin molecules targeting different regions of the SARS-CoV-2 spike protein

The DARPin technology is based on naïve DARPin libraries(*6*), with a physical diversity of about 10^{12} different monovalent DARPin molecules, allowing the selection of sets of very diverse binding molecules by ribosome display(*15, 16*), the method of choice when dealing with libraries of such large diversities. DARPin libraries are based on a consensus design approach using hundreds of ankyrin repeat protein sequences of the human and mouse genome(*17*). An overview of the entire generation process of anti-SARS-CoV-2 spike protein binding DARPin molecules is shown in Figure 1. To obtain individual DARPin molecules binding to distinct domains of the SARS-CoV-2 spike protein and potentially inhibiting viral cell entry, we focused on generating DARPin molecules binding to the receptor binding domain (RBD), the S1 N-terminal domain (NTD) or the S2 domain(*18*). After four ribosome display selection rounds (Figure 1A), we further enriched for the most potently binding DARPin molecules through screening of 3'420 *E. coli* cell extracts overexpressing individual DARPin molecules by homogeneous time-resolved fluorescence (HTRF) assays for binding to different spike protein domains (Figure 1B). Based on binding and ACE2 inhibition profiles obtained in HTRF, which allowed mapping of monovalent DARPin molecules to different spike domains, 380 DARPin molecules were selected to be expressed in 96-well format and purified to homogeneity. DARPin molecules were further characterized for antiviral potency in a VSV-pseudovirion neutralization assay (PsV NA) as well as biophysically by size exclusion chromatography (SEC), Sypro-Orange thermal stability assessment(*19*), ProteOn surface plasmon resonance (SPR) target affinity assessment, and ELISA, to orthogonally evaluate target binding (Figure 1C and D). In parallel to the characterization of the 380 monovalent DARPin molecules, 6 monovalent DARPin molecules of known spike domain specificity were used to randomly assemble a set of 192 tri-specific DARPin molecules (Figure 1E). The antiviral potencies, determined in a PsV-NA screening assay, of these randomly combined tri-specific DARPin molecules provided valuable information on the most potent tri-specific combinations and formats. Based on the combined data for the 380 monovalent DARPin molecules, 11 of them with low pM to low nM affinities, excellent biophysical properties, diversities in amino acid sequences as well as binding for various SARS-CoV-2 spike protein domains (Supplementary Table 1 and Supplementary Figure 1) were selected for the rational generation of 22 multivalent DARPin molecules described below (Figure 1F). After detailed characterization of these 22 multivalent DARPin candidates, systemic exposure was assessed in mice and in Syrian golden hamsters for the most promising multivalent DARPin candidates (Figure 1G). The multivalent DARPin candidate with the longer systemic half-life was evaluated for SARS-CoV-2 protection in a Covid-19 Syrian golden hamster model (Figure 1H).

129 ***Rational design of multivalent DARPin molecules targeting the SARS-CoV-2 spike protein***

130 We aimed to increase virus neutralizing potency through molecular linkage of monovalent DARPin
131 molecules leading to avidity effects. Using the 11 selected mono-specific DARPin molecules, a total of
132 22 multivalent DARPin molecules were generated and characterized in detail, each comprising 3
133 monovalent DARPin molecules against various epitopes of the spike protein as well as two monovalent
134 DARPin molecules binding to human serum albumin (HSA), which have been previously shown to
135 confer long half-life to other DARPin molecules in animals and humans(*7*) (Supplementary Table 2).
136 Each of the 22 multivalent DARPin molecules contained at least one RBD-binding domain since
137 preventing ACE2 receptor interaction is assumed to be the strongest point of interference with virus
138 entering the host cell. Multivalent DARPin molecules were designed to contain several binding
139 modules to RBD (multi-RBD DARPin molecules) or to several distinct domains (multi-mode DARPin
140 molecules). Based on profiling of 22 multivalent DARPin molecules for their biophysical properties and
141 antiviral potency (Supplementary Table 2), we selected two multivalent DARPin molecules,
142 representative for the two different design strategies (i.e. Multi-RBD-DARPin-Candidate, MR-DC, and
143 Multi-Mode-DARPin-Candidate, MM-DC) for further analysis (Figure 2b). DNA sequencing of the
144 individual monovalent DARPin components of MR-DC revealed a similar, but not identical,
145 arrangement of amino acids, suggesting that they share a common mechanism of binding to the RBD.
146 In contrast, the individual components of MM-DC exhibited a high level of sequence diversity,
147 consistent with their different targeting mechanisms (Figure 2c). Neutralization potency for MR-DC
148 and MM-DC was 56 and 36-fold higher in PsV NA, respectively, relative to the most potent neutralizing
149 individual monovalent DARPin that was used for the design of the two types of multivalent DARPin
150 molecules (Figure 2d-e). In addition, IC_{50} values for potency determination in a VSV-SARS-CoV2
151 pseudotype neutralization assay for MR-DC and MM-DC was similar or superior to that of three earlier
152 described potent neutralizing antibodies(*20, 21*). Neutralization assays with the infectious SARS-CoV-
153 2 yielded IC_{50} values of 12 pM for MR-DC (1 ng/ml) and 80 pM for MM-DC (7 ng/ml), respectively
154 (Figure 2f). Still, despite slightly higher potencies displayed by some other screened multi-valent
155 DARPin candidates (e.g. M6, M7, M20 and M22), candidates MR-DC and MM-DC were selected as lead
156 candidates to provide the highest diversity within their paratopes, and potentially the best possible
157 protection against viral escape mutations. In addition, both multivalent DARPin molecules could
158 effectively neutralize pseudotype viruses carrying spike proteins containing natural occurring
159 polymorphisms, including the frequently occurring D614G mutation (Supplementary Table 3). The
160 extremely high neutralization potencies are key for SARS-CoV-2 treatment in particular in a
161 prophylactic setting where very low virus titers at the beginning of the infection are expected.
162
163

164 ***Cryo-EM analysis of monovalent DARPin molecules***

165 To gain further insights into the mode of inhibition and binding, three individual monovalent DARPin
166 molecules targeting RBD, S1-NTD, or S2, were subjected to cryo-electron microscopy (cryo-EM)
167 analysis in complex with the trimeric spike ectodomain. In each case, few intact spikes remained
168 following incubation with the monovalent DARPin molecules, particularly with the S2 binder
169 (Supplementary Figure 2). When spike ectodomains were incubated with RBD-binding monovalent
170 DARPin molecule #3 for 15 seconds prior to vitrification, 3D classification revealed that 65% of the
171 intact S ectodomains were in the closed conformation, 20% had two RBDs in the open conformation
172 and 15% had all three RBDs in the open conformation (Supplementary Figure 3a). For the open RBD
173 classes, additional density, consistent with the size of a monovalent DARPin molecule, was present on
174 the RBD receptor binding ridge (RBR). When the incubation time was increased to 60 seconds, 66% of
175 S ectodomains had three monovalent DARPin-bound RBDs in the open conformation (Supplementary
176 Figure 3b). Interestingly, 18% of the S ectodomains had two DARPin-bound RBDs in the open
177 conformation and one trapped in a partially-closed conformation (Supplementary Figures 3b and 4).
178 These results demonstrate that monovalent DARPin #3 binding prevents closure of the RBD through a
179 previously described ratcheting mechanism(*18*). 3D refinement of the fully open class, from the 60
180 second incubated sample, produced a 4.2 Å global resolution map (Figure 3a and Supplementary
181 Figure 3c-e). The resolution of the map was sufficient to unambiguously assign the pose of RBD-binding
182 monovalent DARPin molecule #3, which binds perpendicular to the RBD receptor binding motif (RBM),
183 with its N-terminus orientated toward the spike three-fold symmetry axis (Figure 3a). The concave
184 DARPin binding surface covers the RBR and overlaps with the ACE2 binding site (Figure 3b). Based on
185 the cryo-EM data, molecular docking experiments were performed. The top scoring model indicated
186 that the interface area is ~700 $Å^2$ and that key epitope residues are F456, Y473, F486, N487 and Y489,
187 which putatively form an interface of hydrophobic interactions and hydrogen-bonds with the DARPin
188 molecule #3 (Supplementary Figure 5). Taken together, these data show that RBD-binding monovalent
189 DARPin molecule #3 inhibits SARS-CoV-2 through receptor functional mimicry, facilitating fusogenic
190 conformational rearrangements of the spike protein. This mechanism of inhibition was also observed
191 for a SARS-CoV neutralizing antibody, S230(*18*), and more recently for a SARS-CoV-2 neutralizing
192 antibody, C105(*22*). Based on our cryo-EM structure, molecular modelling was used to demonstrate
193 that a linker, used in the multivalent DARPin format, would permit simultaneous binding of three RBD-
194 targeting monovalent DARPin molecules (Figure 3c).

195

196 Following a 15 second incubation with the S1-NTD-binding monovalent DARPin molecule #9, 2D
197 classification already revealed clear additional density bound to the spike NTD (Supplementary Figure
198 2). Subsequent 3D classification revealed that most of the DARPin-bound spikes were in the closed

199 conformation, and 19% had one RBD in open conformation (Supplementary Figure 6a). 3D refinement
200 of the fully closed class produced an 8 Å global resolution map (Figure 3d and supplementary Figure
201 6b-c), sufficient to dock and assign the pose of the bound DARPin molecule (Figure 3d). This
202 monovalent DARPin molecule binds to the most distal region of the NTD, which is not resolved in the
203 majority of available spike structures(*13, 23*). However, several spike structures with nearly completely
204 modelled NTDs were recently reported(*24, 25*). The better resolved NTD loops in these structures
205 allowed us to further narrow down the DARPin epitope, indicating that the concave binding surface is
206 ideally situated to interact with the N5 loop, encompassing residues 246-258(*26*) (Figure 3e). A recently
207 described monoclonal antibody, 4A8(*26*), also targets the NTD, involving an extensive hydrophilic
208 interaction network with the N3 loop and, to a lesser extent, the N5 loop. In contrast, molecular
209 docking experiments suggest monovalent DARPin molecule #9 interacts with the NTD primarily with
210 N5 loop residues 248-252 (Supplementary Figure 7), with an interface area of ~600 $Å^2$ and involving
211 both hydrophilic and hydrophobic interactions. Based on our cryo-EM structures, molecular modelling
212 was used to demonstrate that a linker, used in the multivalent DARPin format, would permit
213 simultaneous binding of the NTD and RBD-targeting monovalent DARPin molecules (Figure 3f).
214 Cumulatively, our structural analysis allowed us to generate models of the MR-DC and MM-DC
215 molecules in contact with the spike protein using 3D molecular modeling tools (Supplementary Figure
216 8). In both cases, the half-life extension modules have sufficient space to bind HSA. Within the distance
217 limited by the linker length, we identified a potential binding site for the S2 binder, suggesting that
218 simultaneous binding to the spike protein is feasible. However, structural analysis of S ectodomains
219 incubated with the S2 binder #10 did not reveal any unambiguous density for the bound monovalent
220 DARPin. The low number of intact ectodomains remaining after incubation with monovalent DARPin
221 #10 suggests that, compared to monovalent DARPin molecules #3 and #9, the S2 binder has the
222 greatest destabilizing effect on the structural integrity of the S ectodomains (Supplementary Figure 2).
223

224 ***In vivo antiviral efficacy of a multivalent DARPin in a SARS-CoV-2 hamster infection model***

225 In order to assess the *in vivo* antiviral efficacy of our multivalent DARPin molecule MR-DC, a hamster
226 Covid-19 disease model was performed to study the potential for preventing SARS-CoV-2 related
227 disease (Figure 4a). Syrian golden hamsters (6 females per group) were treated with a single
228 intraperitoneal dose of one multivalent DARPin molecule, MR-DC, using either 16 µg, 160 µg, 1600 µg
229 (per animal; average body weight of ~160g), or with placebo, 24 h prior to intranasal infection with
230 SARS-CoV-2. Readouts included observation of macroscopic assessment of tissues, histopathology,
231 body weight and virus titers. Dose-dependent reduction in tissue damage, immune response to
232 infection, body weight loss, virus titers in throat, nasal turbinates and lung tissue was observed,

233 indicating significant anti-viral activity for the 1600 µg dose and a trend for protection for the 160 µg
234 dose under the conditions of the hamster model (Figure 4b-g).
235 Histopathology results: Intranasal infection with SARS-CoV-2 induced epithelial inflammation and
236 degeneration of the respiratory tract from the nasal turbinates, through the trachea to the
237 bronchi/bronchioles of the lung. More specifically, the inflammation comprised a mixed inflammatory
238 cell infiltrate of lymphocytes, macrophages, plasma, cells and granulocytes which was variably
239 accompanied by epithelial degeneration, regeneration, disorganization, single cell necrosis and
240 inflammatory exudates in the bronchial lumen and nasal cavity. In the lung of more severely affected
241 animals the inflammation extended from the bronchial epithelium to adjacent alveolar interstitium,
242 alveolar sacs and blood vessels (with or without perivascular edema); prominent Type II alveolar
243 pneumocytes and variable hemorrhage were also variably present within the lesion. These findings
244 were most severe in SARS-CoV-2 infected animals receiving the vehicle and the lowest dose of 16ug
245 multivalent DARPin MR-DC. While there was some reduction in the severity of the lesion in infected
246 animals given 160 ug, there was a significant improvement in animals treated with the highest dose of
247 1600 ug (Figure 4b; Supplementary Figure 9).
248 SARS-CoV-2 infection was accompanied by a reactive change in lymphoid organs consistent with
249 immune activation. Activation of germinal centers was accompanied by increased cellularity of the
250 white pulp in the spleen and increased cellularity of the medullary sinuses (macrophages and plasma
251 cells) in the mandibular lymph node. Again, these findings were generally more apparent in infected
252 animals receiving the vehicle, with a dose-related decrease in severity in MR-DC-treated groups,
253 particularly in animals treated with the highest dose of 1600 ug (Figure 4c; Supplementary Figure 9).
254 The pharmacokinetics for MR-DC, injected at 160 µg and 1600 µg per animal, was evaluated in an
255 independent study in non-infected Syrian golden hamsters, proving systemic exposure for the duration
256 of the in-life phase of this hamster PD model (Supplementary Figure 10).

257 **Discussion**

258 Multiple strategies to combat the COVID-19 pandemic are urgently needed. Next to preventive
259 vaccination approaches, monoclonal antibodies are showing therapeutic promise, based on highly
260 potent virus inhibition and encouraging animal and clinical efficacy(*27-29*). However, due to the global
261 need for COVID-19, manufacturing is expected to become a major bottleneck for vaccines and
262 antibodies. A number of alternative molecules are being developed to complement and partially
263 overcome this limitation of antibodies. Here we describe the generation of DARPin molecules - one
264 prominent alternative to antibodies(*30*) amongst others(*31-34*) - that bind the SARS-CoV-2 spike
265 protein. We tested a library of one trillion DARPin molecules and identified multiple DARPin molecules
266 with different functionalities and binding specificities. By molecular linkage of individual DARPin
267 molecules, we developed multivalent DARPin molecules with low picomolar neutralizing activity and
268 demonstrated their protective efficacy against SARS-CoV-2 infection in a hamster model. In particular,
269 reduced lung tissue damage and reduced virus replication in the lower and upper respiratory tract
270 were observed, the latter also being important for reducing virus shedding and transmission. The most
271 advanced of those multivalent DARPin molecules, MP0420 or ensovibep, is currently being studied in
272 Phase 2.

273

274 The most potent neutralizing monovalent DARPin molecules were found to target the RBD, blocking
275 the spike-ACE2 interaction necessary for infection. This finding is congruent with the identified
276 epitopes of potent neutralizing antibodies obtained from COVID-19 patients(*20, 35-39*). Thus, the *in*
277 *vitro* approach using DARPin molecules independently confirms that the ACE2 interaction site on the
278 SARS-CoV-2 spike protein is one of the most vulnerable sites to block virus infection in cell culture.
279 The single-chain binding domain nature of DARPin molecules facilitated the design of multiparatopic
280 and multispecific DARPin molecules with greatly increased neutralization potencies. Virus
281 neutralization capacity increased substantially when three DARPin molecules were linked - relative to
282 the individual modules - likely due to both, increased avidity when binding to the trimeric spike
283 proteins as well as multiple spike domains. A similar strategy with comparable outcome has been
284 recently described for nanobodies. The observed *in vitro* neutralization capacity of the multivalent
285 DARPin molecules in the low picomolar range is similar to or even outcompetes the neutralizing
286 capacities of monoclonal antibodies. The protection against SARS-CoV-2 infections demonstrated in a
287 hamster model at 1600 mg per animal (10 mg/kg) and the partial protection at 160 mg (1 mg/kg) is in
288 the range reported for monoclonal antibodies(*27, 31, 37, 40, 41*).

289

290 The multivalent DARPin molecules are expected to retain potency even if the spike protein of SARS-
291 CoV-2 should mutate considerably in the future, especially when multiple modes of action are

292 addressed. Evaluation of the impact of a panel of reported mutations in the SARS-CoV-2 spike protein
293 revealed no loss of neutralizing capacity of our lead candidates in a PsV NA and a set of emerging
294 variants and spike protein mutations were recently reported elsewhere(*42*). Although it remains to be
295 determined if additional mutations will impact the neutralization potencies of the multivalent DARPin
296 molecules, we expect multivalent DARPin molecules to retain high potency in case the SARS-CoV-2
297 spike protein should mutate in the future.
298
299 DARPin molecules(*30*) have shown good promise for both ophthalmology and oncology patients.
300 Within oncology, MP0250 is the DARPin molecule(*7*) with most systemic data available to date:
301 MP0250 is a dual inhibitor of VEGF and HGF and is being developed for multiple myeloma in
302 combination with small molecules. MP0250 shows a long systemic half-life of about 2 weeks in human,
303 low immunogenicity potential, and has been given to individual patients for more than two years. All
304 42 patients in a phase I clinical trial maintained systemic exposure after repeated dosing while 2
305 patients, out of these 42 patients, showed elevated anti-drug antibodies which did not affect MP0250
306 exposure. Here, we demonstrate prophylactic protection from SARS-CoV-2 infection by a multivalent
307 DARPin molecule in a hamster model. Reported systemic exposures, achieved with human serum
308 albumin binding DARPin molecules, appear comparable to the half-lives reported for monoclonal
309 antibodies. Due to the lack of an immune stimulating Fc-fragment, we envision no generation of
310 antibody dependent enhancement (ADE) effects, a potential side-effect of monoclonal antibodies in
311 patients with inflamed lungs(*43-46*). This hypothetical differentiation, when compared to monoclonal
312 antibody treatments including immune stimulating Fc-fragments, is currently under clinical
313 investigation and remains to be verified.
314
315 Generally, DARPin molecules demonstrate excellent temperature stability, which might enable
316 alternative routes of administration, such as inhalation described for other highly stable protein
317 scaffolds(*47, 48*). The simple molecular architecture of multivalent DARPin molecules allows
318 manufacturing in bacterial expression systems at very high yields which leads to cost-effective and
319 scalable production of antiviral biologicals at industrial quantities (supplementary table 5).
320 Consequently, global access to this novel class of therapeutics may be highly additive to monoclonal
321 antibody approaches and thus contribute to overcoming the COVID-19 pandemic(*49*). We anticipate
322 that the presented workflow for DARPin development can be applied for any future emerging
323 (corona)virus. We have proven that high-affinity binding and potently neutralizing DARPin molecules
324 can be developed in a matter of weeks, without the requirement of immunization of animals or access
325 to patient materials. Such fast track development strategies of picomolar inhibitors are critical to raise
326 preparedness level towards novel pandemic viruses.

327 **Data availability**

328 The EM density maps for the SARS-CoV-2 spike ectodomain in complex with monovalent DARPin #3
329 (state 1 and state 2), and monovalent DARPin #9 have been deposited to the Electron Microscopy Data
330 Bank under the accession codes EMD-11953, EMD-11954 and EMD-11956, respectively. The
331 monovalent DARPin and multivalent DARPin sequences, and pseudo-atomic models derived from
332 molecular docking experiments, are available (by contacting the corresponding author) for research
333 purposes only under an MTA, which allows the use of the data for non-commercial purposes but not
334 their disclosure to third parties.

335

336 **Acknowledgements**

337 We would particularly like to thank those colleagues at Molecular Partners who are not included in the
338 author list and are currently advancing the program through the clinic. Additionally, we would like to
339 thank William Lee, former board member of Molecular Partners - and the Virology group at Gilead
340 Sciences for their helpful input. The authors also thank Dr. Gert Zimmer for the gift of the recombinant
341 VSV (Institute of Virology and Immunology (IVI), CH-3147 Mittelhäusern, Switzerland, Department of
342 Infectious Diseases and Pathobiology, Vetsuisse Faculty, University of Bern, CH-3012 Bern,
343 Switzerland). The expression plasmid for the SARS-CoV-2 spike protein was kindly provided by Dr.
344 Giulia Torriani and Dr. Isabella Eckerle (Department of Medicine, University of Geneva, Switzerland).
345 SR & JM were supported by Swiss Federal Office for Civil Protection (Grants Nr. 353008564/Stm,
346 353008218/Stm, and 353008560/Stm to Olivier Engler and Stefan Kunz).
347 We would like to thank for the supply of the two 2019-nCoV strains: i) 2019-nCoV/IDF0372/2020
348 provided by the National Reference Centre for Respiratory Viruses hosted by Institut Pasteur (Paris,
349 France) and headed by Dr. Sylvie van der Werf as well as the human sample from which strain 2019-
350 nCoV/IDF0372/2020 was isolated, provided by Dr. X. Lescure and Pr. Y. Yazdanpanah from the Bichat
351 Hospital.
352 D.L.H. is funded from by the European Union's Horizon 2020 research and innovation program under
353 the Marie Skłodowska-Curie grant agreement (No 842333) and holds an EMBO non-stipendiary long-
354 term Fellowship (ALTF 1172-2018). Cryo-EM data processing was carried out on the Dutch national
355 e-infrastructure with the support of SURF Cooperative.

356

357 **Funding**

358 All studies were funded by Molecular Partners AG, Switzerland.

359

360 **Author contributions**

361 M.W., S.R., D.L.H., V.C., C.R., S.F., A.Z., N.V., K.M.D., C.Z., M.A.H., L.d.W., K.J.S., F.J.M.v.K., O.E. , B.-J. B.,
362 M.T.S.; P.A.: conceptualized and designed experiments; M.W., S.R., D.L.H., A.S., D.V., M.P., T.H., A.N.,
363 A.C., P.S., M.M., M.H., M.F., Y.K., I.S., C.I., T.L., S.M., C.H., D.S., A.B., A.L., T.V., G.S., K.P., M.S., J.M.,
364 S.Ry., S.T., H.L., C.W., W.L., I.D.: performed laboratory experiments; D.L.H., C.R, F.R.: performed
365 computational work; M.W., S.R., D.L.H., H.K.B., S.L., S.F., F.J.M.v.K., O.E., B.-J. B., M.T.S., P.A. drafted
366 the manuscript. S.L., D.S., M.T.S., P.A. acquired funding. All authors reviewed the manuscript.

367

368 **Competing interests:** Molecular Partners authors own performance share units and/or stock of the
369 company. HKB owns stock of the company.

370

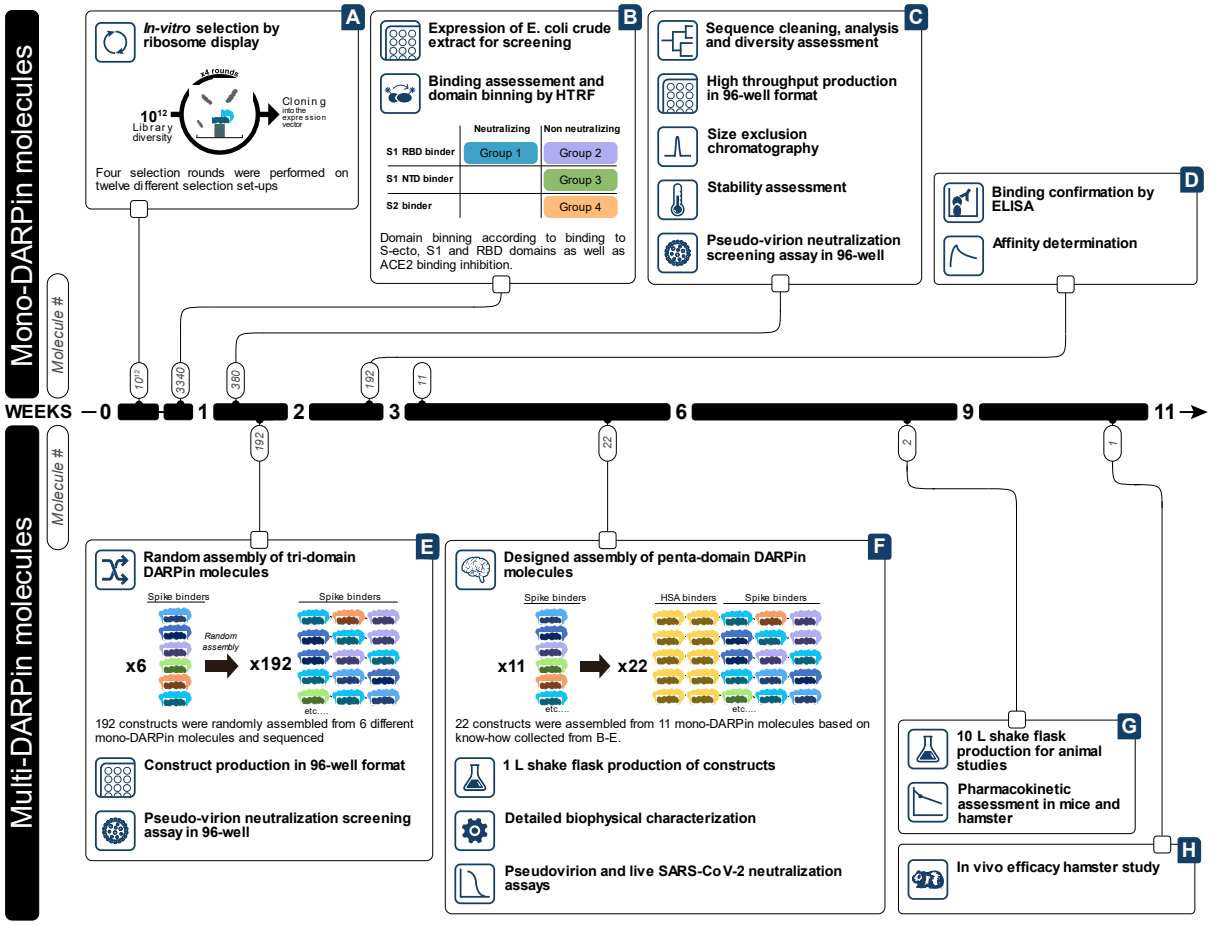

Figure 1: **Process overview for the generation of anti-SARS-CoV-2 multivalent DARPin molecules.** Upper panel, generation and evaluation of monovalent DARPin molecules. Lower panel, assembly and deep-characterization of multivalent DARPin molecules.

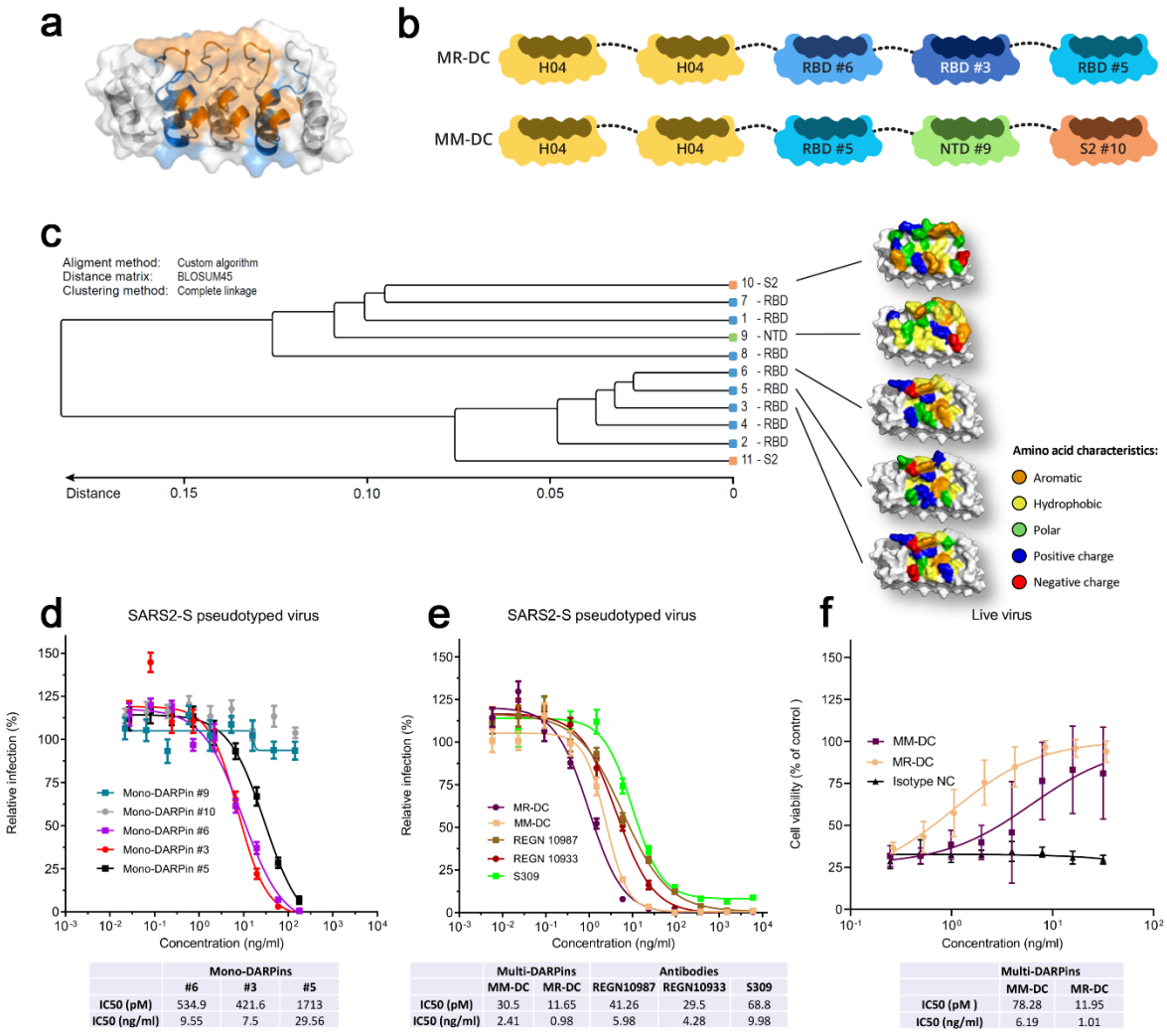

	Mono-DARPins		
	#6	#3	#5
IC50 (pM)	534.9	421.6	1713
IC50 (ng/ml)	9.55	7.5	29.56

	Multi-DARPins		Antibodies		
	MM-DC	MR-DC	REGN10987	REGN10933	S309
IC50 (pM)	30.5	11.65	41.26	29.5	68.8
IC50 (ng/ml)	2.41	0.98	5.98	4.28	9.98

	Multi-DARPins	
	MM-DC	MR-DC
IC50 (pM)	78.28	11.95
IC50 (ng/ml)	6.19	1.01

Figure 2: Architecture, diversity and *in vitro* potency of two multivalent DARPin molecules. a) Ribbon structure and semi-transparent surface representation of a monovalent DARPin molecule. The designed ankyrin repeats are colored alternatingly in white and blue for the five repeats. The randomized residues present in the rigid target binding surface are colored orange. b) Schematic overview of the MR-DC and MM-DC constructs. Protein linkers are depicted as gray dashed lines and the half-life extending human serum albumin binding monovalent DARPin (H) is colored yellow. c) Sequence family tree illustrating the sequence diversity amongst the 11 monovalent DARPin molecules chosen for the generation of multivalent DARPin molecules. Surface representations of five Monovalent DARPin molecules binding to the RBD, NTD or S2 are shown, with the amino acid residues in the binding surface colored according to their biophysical characteristics as indicated. d, e) DARPin- respectively antibody-mediated neutralization of infection of luciferase-encoding VSV particles pseudotyped with the SARS-CoV-2 spike protein. Pseudotype VSV particles pre-incubated with monovalent DARPin molecules (d), multivalent DARPin molecules (MM-DC and MR-DC) or control antibodies (e) at the indicated concentrations were used to infect VeroE6 cells. Luciferase activities in cell lysates were determined at 24 h post transduction to calculate infection (%) relative to mock-

391 treated virus controls. The average ± SD from two independent experiments performed in sextuplicate
392 is shown. f) Multivalent DARPin-mediated cell protection of SARS-CoV-2 infection. SARS-CoV-2 pre-
393 incubated with multivalent DARPin molecules MM-DC or MR-DC, or with isotype negative control
394 (isotype NC) at the indicated concentrations were used to infect VeroE6 cells. Cell viability was
395 determined using the CellTiter-Glo luminescent cell viability assay and represented as relative (%) to
396 mock infected cells. Half-maximal inhibitory concentration values (IC_{50}) of DARPin molecules and
397 antibodies are indicated in the lower panel tables (d-f).

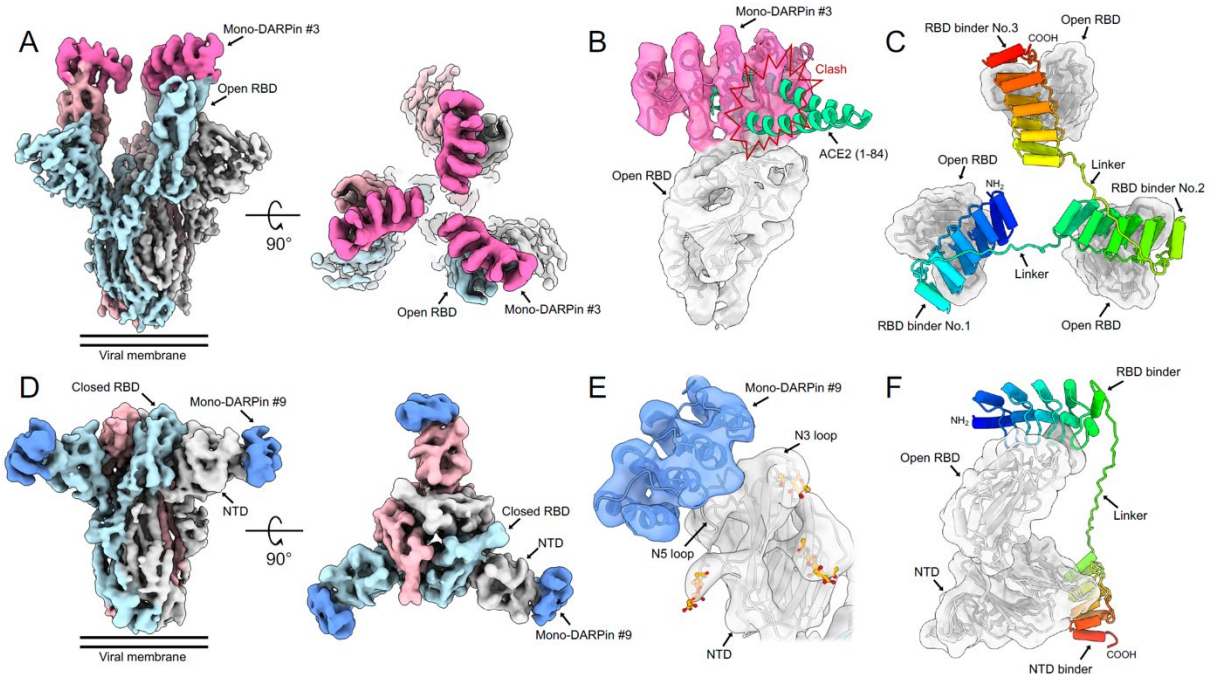

Figure 3: Cryo-EM analysis of monovalent DARPin molecules. A) Cryo-EM density for the SARS-CoV-2 spike ectodomain in complex with the RBD targeting monovalent DARPin #3, shown as two orthogonal views. The DARPin density is colored magenta and the three spike protomers are colored light blue, grey and pink. B) Zoomed in view of a single DARPin #3-bound RBD with the cryo-EM density shown semi-transparent. The atomic coordinates for the fitted fully open spike (PDB ID: 6XCN) and the DARPin homology model are overlaid. The atomic coordinates for residues 1-84 of the RBD bound ACE2 (PDB ID: 6M0J), colored green, is superimposed. C) Proposed model of three covalently linked RBD-targeting monovalent DARPin molecules shown in a rainbow color scheme from the N terminus (blue) to the C terminus (red). D) Cryo-EM density for the SARS-CoV-2 spike ectodomain in complex with the NTD targeting monovalent DARPin #9, shown as two orthogonal views. The mono-DARPin #9 density is colored blue and the three spike protomers are colored light blue, grey and pink. E) Zoomed in view of the DARPin molecule #9 bound to the NTD with the cryo-EM density shown semi-transparent. The atomic coordinates for the fitted fully closed spike (PDB ID: 6ZGE) and the DARPin homology model are overlaid and colored grey and blue, respectively. The N3 and N5 loops are labelled and glycans are shown in stick representation and colored orange. F) Proposed model of the covalently linked NTD and RBD targeting monovalent DARPin molecules, shown in a rainbow color scheme from the N terminus (blue) to the C terminus (red).

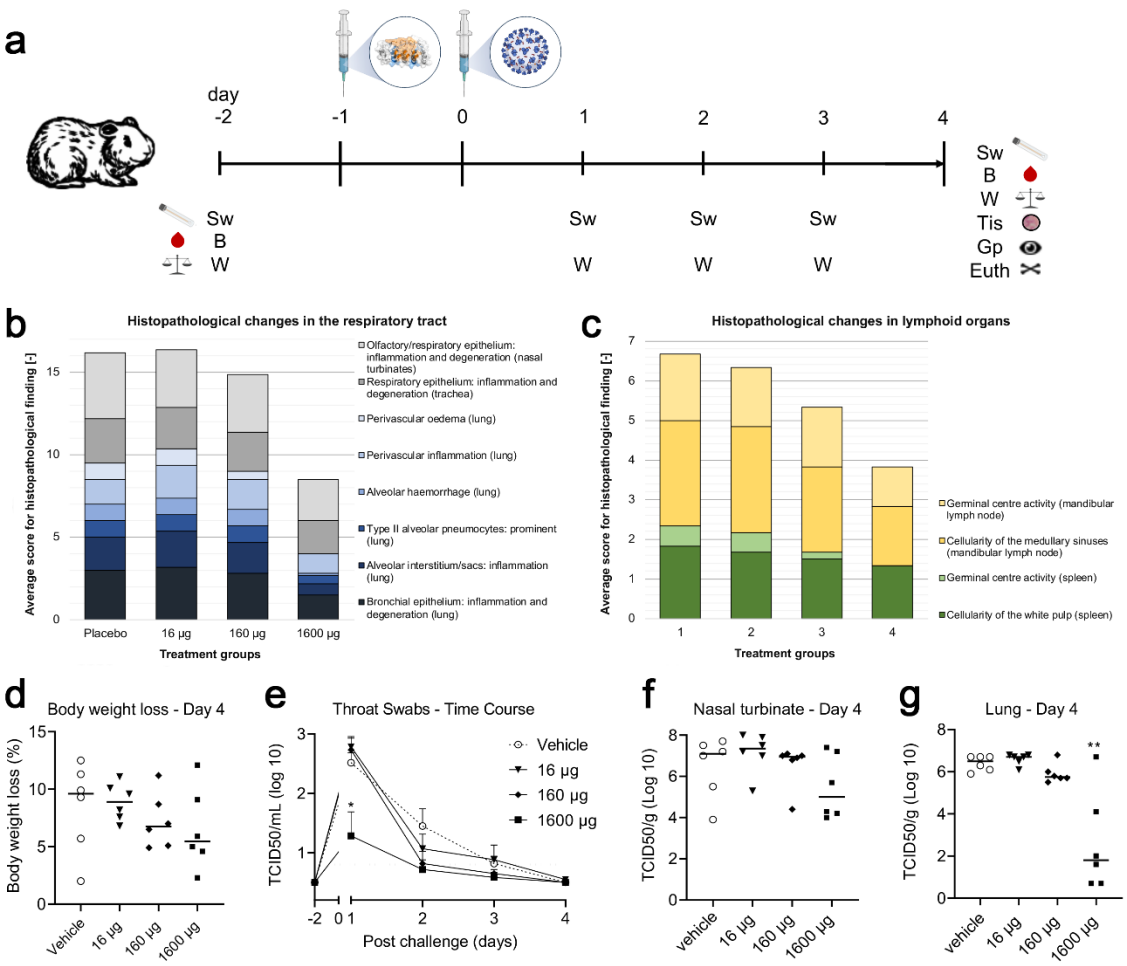

Figure 4: In-vivo efficacy of MR-DC in treating SARS-CoV-2 infection in a preventive Syrian golden hamster model. a) study design: six animals were used per dose group. Generally high variations were observed in control and treatment groups. At Day -2, body weight (W) was measured, blood (B) was taken, and the first throat swab (Sw) performed. Animals were euthanized on Day 4 and tissue (Tis) were taken and gross pathology (Gp) was performed. (b) Histopathological changes in the respiratory tract (lung - blue bars, trachea and nasal turbinates – grey bars). (c) Histopathological changes in lymphoid organs (spleen - green bars, mandibular lymph nodes - yellow bars). A trend to dose-dependent reduction of body-weight loss at day 4 (d), virus titers post challenge for throat swabs (e), nasal turbinate (f) and significant reduction of viral loads in the lung at 1600 µg (10 mg/kg), with two animals below detection limit, as well as a trend to dose-dependent reduction of viral loads at 160 µg (1 mg/kg) (g). Statistically significant differences between Placebo and 1600 µg group: *T-test; P value = 0.0183 / **T-test; P value = 0.0031.

430 **References**

431 1. P. Zhou *et al.*, A pneumonia outbreak associated with a new coronavirus of probable
432 bat origin. *Nature* **579**, 270-273 (2020).
433 2. S. Hsiang *et al.*, The effect of large-scale anti-contagion policies on the COVID-19
434 pandemic. *Nature* **584**, 262-267 (2020).
435 3. S. Flaxman *et al.*, Estimating the effects of non-pharmaceutical interventions on
436 COVID-19 in Europe. *Nature* **584**, 257-261 (2020).
437 4. R. K. Guy, R. S. DiPaola, F. Romanelli, R. E. Dutch, Rapid repurposing of drugs for
438 COVID-19. *Science* **368**, 829-830 (2020).
439 5. H. Ledford, Antibody therapies could be a bridge to a coronavirus vaccine - but will
440 the world benefit? *Nature* **584**, 333-334 (2020).
441 6. H. K. Binz *et al.*, High-affinity binders selected from designed ankyrin repeat protein
442 libraries. *Nat Biotechnol* **22**, 575-582 (2004).
443 7. R. D. Baird *et al.*, First-in-Human Phase I Study of MP0250, a First-in-Class DARPin
444 Drug Candidate Targeting VEGF and HGF, in Patients With Advanced Solid Tumors. *J*
445 *Clin Oncol* **39**, 145-154 (2021).
446 8. J. Shang *et al.*, Structural basis of receptor recognition by SARS-CoV-2. *Nature* **581**,
447 221-224 (2020).
448 9. M. A. Tortorici, D. Veesler, Structural insights into coronavirus entry. *Adv Virus Res*
449 **105**, 93-116 (2019).
450 10. M. Letko, A. Marzi, V. Munster, Functional assessment of cell entry and receptor
451 usage for SARS-CoV-2 and other lineage B betacoronaviruses. *Nat Microbiol* **5**, 562-
452 569 (2020).
453 11. M. Hoffmann *et al.*, SARS-CoV-2 Cell Entry Depends on ACE2 and TMPRSS2 and Is
454 Blocked by a Clinically Proven Protease Inhibitor. *Cell* **181**, 271-280 e278 (2020).
455 12. A. C. Walls *et al.*, Cryo-electron microscopy structure of a coronavirus spike
456 glycoprotein trimer. *Nature* **531**, 114-117 (2016).
457 13. A. C. Walls *et al.*, Structure, Function, and Antigenicity of the SARS-CoV-2 Spike
458 Glycoprotein. *Cell* **181**, 281-292 e286 (2020).
459 14. A. C. Walls *et al.*, Tectonic conformational changes of a coronavirus spike
460 glycoprotein promote membrane fusion. *Proc Natl Acad Sci U S A* **114**, 11157-11162
461 (2017).
462 15. C. Zahnd, P. Amstutz, A. Pluckthun, Ribosome display: selecting and evolving proteins
463 in vitro that specifically bind to a target. *Nat Methods* **4**, 269-279 (2007).
464 16. J. Hanes, L. Jermutus, S. Weber-Bornhauser, H. R. Bosshard, A. Pluckthun, Ribosome
465 display efficiently selects and evolves high-affinity antibodies in vitro from immune
466 libraries. *Proc Natl Acad Sci U S A* **95**, 14130-14135 (1998).
467 17. H. K. Binz, M. T. Stumpp, P. Forrer, P. Amstutz, A. Pluckthun, Designing repeat
468 proteins: well-expressed, soluble and stable proteins from combinatorial libraries of
469 consensus ankyrin repeat proteins. *J Mol Biol* **332**, 489-503 (2003).
470 18. A. C. Walls *et al.*, Unexpected Receptor Functional Mimicry Elucidates Activation of
471 Coronavirus Fusion. *Cell* **176**, 1026-1039 e1015 (2019).
472 19. F. H. Niesen, H. Berglund, M. Vedadi, The use of differential scanning fluorimetry to
473 detect ligand interactions that promote protein stability. *Nat Protoc* **2**, 2212-2221
474 (2007).
475 20. J. Hansen *et al.*, Studies in humanized mice and convalescent humans yield a SARS-
476 CoV-2 antibody cocktail. *Science* **369**, 1010-1014 (2020).

477 21. D. Pinto *et al.*, Cross-neutralization of SARS-CoV-2 by a human monoclonal SARS-CoV
478 antibody. *Nature* **583**, 290-295 (2020).
479 22. C. O. Barnes *et al.*, Structures of Human Antibodies Bound to SARS-CoV-2 Spike
480 Reveal Common Epitopes and Recurrent Features of Antibodies. *Cell* **182**, 828-842
481 e816 (2020).
482 23. D. Wrapp *et al.*, Cryo-EM structure of the 2019-nCoV spike in the prefusion
483 conformation. *Science* **367**, 1260-1263 (2020).
484 24. A. G. Wrobel *et al.*, SARS-CoV-2 and bat RaTG13 spike glycoprotein structures inform
485 on virus evolution and furin-cleavage effects. *Nat Struct Mol Biol* **27**, 763-767 (2020).
486 25. Y. Cai *et al.*, Distinct conformational states of SARS-CoV-2 spike protein. *Science* **369**,
487 1586-1592 (2020).
488 26. X. Chi *et al.*, A neutralizing human antibody binds to the N-terminal domain of the
489 Spike protein of SARS-CoV-2. *Science* **369**, 650-655 (2020).
490 27. A. Baum *et al.*, REGN-COV2 antibodies prevent and treat SARS-CoV-2 infection in
491 rhesus macaques and hamsters. *Science* **370**, 1110-1115 (2020).
492 28. P. Chen *et al.*, SARS-CoV-2 Neutralizing Antibody LY-CoV555 in Outpatients with
493 Covid-19. *N Engl J Med* **384**, 229-237 (2021).
494 29. B. E. Jones *et al.*, LY-CoV555, a rapidly isolated potent neutralizing antibody, provides
495 protection in a non-human primate model of SARS-CoV-2 infection. *bioRxiv*, (2020).
496 30. M. T. Stumpp, K. M. Dawson, H. K. Binz, Beyond Antibodies: The DARPin((R)) Drug
497 Platform. *BioDrugs* **34**, 423-433 (2020).
498 31. M. Schoof *et al.*, An ultrapotent synthetic nanobody neutralizes SARS-CoV-2 by
499 stabilizing inactive Spike. *Science* **370**, 1473-1479 (2020).
500 32. L. Cao *et al.*, De novo design of picomolar SARS-CoV-2 miniprotein inhibitors. *Science*
501 **370**, 426-431 (2020).
502 33. T. W. Linsky *et al.*, De novo design of potent and resilient hACE2 decoys to neutralize
503 SARS-CoV-2. *Science* **370**, 1208-1214 (2020).
504 34. J. D. Walter, C. A. J. Hutter, A. A. Garaeva, M. Scherer, I. Zimmermann, Highly potent
505 bispecific sybodies neutralize SARS-CoV-2. *bioRxiv*, (2020).
506 35. P. J. M. Brouwer *et al.*, Potent neutralizing antibodies from COVID-19 patients define
507 multiple targets of vulnerability. *Science* **369**, 643-650 (2020).
508 36. L. Liu *et al.*, Potent neutralizing antibodies against multiple epitopes on SARS-CoV-2
509 spike. *Nature* **584**, 450-456 (2020).
510 37. T. F. Rogers *et al.*, Isolation of potent SARS-CoV-2 neutralizing antibodies and
511 protection from disease in a small animal model. *Science* **369**, 956-963 (2020).
512 38. R. Shi *et al.*, A human neutralizing antibody targets the receptor-binding site of SARS-
513 CoV-2. *Nature* **584**, 120-124 (2020).
514 39. S. J. Zost *et al.*, Potently neutralizing and protective human antibodies against SARS-
515 CoV-2. *Nature* **584**, 443-449 (2020).
516 40. J. Kreye *et al.*, A Therapeutic Non-self-reactive SARS-CoV-2 Antibody Protects from
517 Lung Pathology in a COVID-19 Hamster Model. *Cell* **183**, 1058-1069 e1019 (2020).
518 41. B. L. Haagmans *et al.*, SARS-CoV-2 neutralizing human antibodies protect against
519 lower respiratory tract disease in a hamster model. *bioRxiv*, (2020).
520 42. S. Rothenberger, M. Walser, Multi-specific DARPin® therapeutics demonstrate very
521 high potency against mutated SARS-CoV-2 variants in vitro. *bioRxiv*.
522 43. L. Liu *et al.*, Anti-spike IgG causes severe acute lung injury by skewing macrophage
523 responses during acute SARS-CoV infection. *JCI Insight* **4**, (2019).

524 44. A. M. Arvin *et al.*, A perspective on potential antibody-dependent enhancement of
525 SARS-CoV-2. *Nature* **584**, 353-363 (2020).
526 45. A. Renn, Y. Fu, X. Hu, M. D. Hall, A. Simeonov, Fruitful Neutralizing Antibody Pipeline
527 Brings Hope To Defeat SARS-Cov-2. *Trends Pharmacol Sci* **41**, 815-829 (2020).
528 46. T. Zohar, G. Alter, Dissecting antibody-mediated protection against SARS-CoV-2. *Nat*
529 *Rev Immunol* **20**, 392-394 (2020).
530 47. S. Nambulli *et al.*, Inhalable Nanobody (PiN-21) prevents and treats SARS-CoV-2
531 infections in Syrian hamsters at ultra-low doses. *bioRxiv*, (2021).
532 48. A. A. Matthews, P. L. R. Ee, R. Ge, Developing inhaled protein therapeutics for lung
533 diseases. *Molecular Biomedicine* **1**, 1-14 (2020).
534 49. H. Ledford, The race to make COVID antibody therapies cheaper and more potent.
535 *Nature* **587**, 18 (2020).
536 50. H. K. Binz *et al.*, Design and characterization of MP0250, a tri-specific anti-HGF/anti-
537 VEGF DARPin(R) drug candidate. *MAbs* **9**, 1262-1269 (2017).
538 51. G. Torriani *et al.*, Macropinocytosis contributes to hantavirus entry into human
539 airway epithelial cells. *Virology* **531**, 57-68 (2019).
540 52. C. Wang *et al.*, A human monoclonal antibody blocking SARS-CoV-2 infection. *Nat*
541 *Commun* **11**, 2251 (2020).
542 53. J. Zivanov *et al.*, New tools for automated high-resolution cryo-EM structure
543 determination in RELION-3. *Elife* **7**, (2018).
544 54. S. Q. Zheng *et al.*, MotionCor2: anisotropic correction of beam-induced motion for
545 improved cryo-electron microscopy. *Nat Methods* **14**, 331-332 (2017).
546 55. K. Zhang, Gctf: Real-time CTF determination and correction. *J Struct Biol* **193**, 1-12
547 (2016).
548 56. E. F. Pettersen *et al.*, UCSF Chimera--a visualization system for exploratory research
549 and analysis. *J Comput Chem* **25**, 1605-1612 (2004).
550 57. R. Sanchez-Garcia *et al.*, DeepEMhancer: a deep learning solution for cryo-EM
551 volume post-processing. *bioRxiv*, (2020).
552 58. M. A. Cianfrocco, M. Wong, C. Youn, R. Wagner, paper presented at the The Practice
553 and Experience in Advanced Research Computing, New Orleans, LA 2017.
554 59. A. Leaver-Fay *et al.*, ROSETTA3: an object-oriented software suite for the simulation
555 and design of macromolecules. *Methods Enzymol* **487**, 545-574 (2011).
556 60. P. S. Huang *et al.*, RosettaRemodel: a generalized framework for flexible backbone
557 protein design. *PLoS One* **6**, e24109 (2011).
558 61. L. G. Nivon, R. Moretti, D. Baker, A Pareto-optimal refinement method for protein
559 design scaffolds. *PLoS One* **8**, e59004 (2013).
560 62. D. L. Hurdiss *et al.*, Cryo-EM structure of coronavirus-HKU1 haemagglutinin esterase
561 reveals architectural changes arising from prolonged circulation in humans. *Nat*
562 *Commun* **11**, 4646 (2020).
563 63. S. Chaudhury *et al.*, Benchmarking and analysis of protein docking performance in
564 Rosetta v3.2. *PLoS One* **6**, e22477 (2011).
565 64. A. C. Wallace, R. A. Laskowski, J. M. Thornton, LIGPLOT: a program to generate
566 schematic diagrams of protein-ligand interactions. *Protein Eng* **8**, 127-134 (1995).
567 65. T. D. Goddard *et al.*, UCSF ChimeraX: Meeting modern challenges in visualization and
568 analysis. *Protein Sci* **27**, 14-25 (2018).
569 66. A. Morin *et al.*, Collaboration gets the most out of software. *Elife* **2**, e01456 (2013).
570 67. R. A. Laskowski, M. B. Swindells, LigPlot+: multiple ligand-protein interaction
571 diagrams for drug discovery. *J Chem Inf Model* **51**, 2778-2786 (2011).
572

573

574

575

576 # Supplementary Materials for

577

578

579 # Highly potent anti-SARS-CoV-2 multivalent DARPin

580 # therapeutic candidates

581

582 **Walser et al.**

583

584

585

586

587

588

589

590

591

592

593 ## Materials and Methods

594 *SARS-CoV-2 spike proteins variants used*

595 Proteins used for selections comprised SARS-CoV-2 S protein ectodomain (SARS2-Secto-d72-GCN4-
596 Streptag; University of Utrecht), SARS-CoV-2 S protein (S1+S2 ECT, His-tag; Sinobiological 40589-
597 V08B1), Bio-COVID-19_S1 protein_His_Avitag (Acro Biosystems), SARS2-S1-Flag-3Streptag (University
598 of Utrecht), COVID-19_S_protein_RBD_Fc (Acro Biosystems), and SARS2-S1B-2Streptag (University of
599 Utrecht). Proteins were biotinylated by using standard methods.

600

601 *Selection of SARS-CoV-2 spike protein-specific DARPin molecules by ribosome display*

602 DARPin libraries(*6*) (N2C and N3C) were used in ribosome display selections(*15, 16*) against the SARS-
603 CoV-2 spike protein variants. Four selection rounds were performed per target and per library using
604 decreasing target concentrations and increasing washing stringency (wash buffer composition: 50 mM
605 Tris-HOAc (pH 7.5 at 4°C), 150 mM NaCl, 50 mM $Mg(OAc)_2$, 0.05% Tween-20), to increase selection
606 pressure from round 1 to round 4. The number of reverse transcription (RT)-PCR cycles after each
607 selection round was continuously reduced, adjusting to the selection yield due to enrichment of high
608 affinity binders. In detail, the following panning conditions were applied: RD panning round 1: 400 nM
609 target concentration, 8 washes for 1 minutes in wash buffer, 45 PCR cycles; RD panning round 2: 100
610 nM target concentration, 3 washes for 1 minute in wash buffer, then 3 washes for 15 minutes in wash
611 buffer, followed by 2 washes for 1 minute in wash buffer, 35 PCR cycles; RD panning round 3: 25 nM
612 target concentration, 3 washes for 1 minute in wash buffer, then 3 washes for 30 minutes in wash
613 buffer, followed by 2 washes for 1 minute in wash buffer, 30 PCR cycles; RD panning round 4: 5 nM
614 target concentration, 3 washes for 1 minute in wash buffer, then 3 washes for 45 minutes in wash
615 buffer, followed by 2 washes for 1 minute in wash buffer, 35 PCR cycles (for sub-cloning purposes into
616 expression vector). The 12 resulting pools were then subjected to a binder screening.

617

618 *Screening of monovalent DARPin molecules*

619 Monovalent DARPin molecules specifically binding to the S1-RBD, S1-NTD and S2 domains of the spike
620 protein of SARS-CoV-2 in solution were identified by a homogeneous time resolved fluorescence
621 (HTRF) assay using crude extracts of DARPin-expressing *Escherichia coli* (*E. coli*) cells using standard
622 protocols Briefly, DARPin clones selected by ribosome display were cloned into a derivative of the
623 pQE30 (Qiagen) expression vector, *E. coli* XL1-Blue (Stratagene) was transformed and plated on LB-
624 agar (containing 1% glucose and 50 µg/ml ampicillin) and then incubated overnight at 37°C. Single
625 colonies were picked into individual wells of 96 well plates containing 165 µl growth medium (LB
626 containing 1% glucose and 50 µg/ml ampicillin) and incubated overnight at 37°C, shaking at 800 rpm.

627 150 µl of fresh LB medium containing 50 µg/ml ampicillin was inoculated with 8.5 µl of the overnight
628 culture in a fresh 96-deep-well plate. After incubation for 120 min at 37°C and 850 rpm, expression
629 was induced with IPTG (0.5 mM final concentration) and continued for 6 h. Cells were harvested by
630 centrifugation of the 96-deep-well plates, supernatant was discarded, and the pellets were frozen at
631 -20°C overnight before resuspension in 8.5 µl B-PERII (Thermo Scientific) and incubation for 1 h at
632 room temperature with shaking (600 rpm). Then, 160 µl PBS was added and cell debris was removed
633 by centrifugation (3220 g for 15 min). The extract of each lysed clone was applied as a 1:200 dilution
634 (final concentration) in PBSTB (PBS supplemented with 0.1% Tween 20® and 0.2% (w/v) BSA, pH 7.4)
635 together with 20 nM (final concentration) biotinylated spike protein domain, 1:400 (final
636 concentration) of anti-6His-D2 HTRF antibody – FRET acceptor conjugate (Cisbio) and 1:400 (final
637 concentration) of anti-strep-Tb antibody FRET donor conjugate (Cisbio, France) to a well of a 384-well
638 plate and incubated for 120 min at 4°C. The HTRF was read-out on a Tecan M1000 using a 340 nm
639 excitation wavelength and a 620±10 nm emission filter for background fluorescence detection and a
640 665±10 nm emission filter to detect the fluorescence signal for specific binding. The extract of each
641 lysed clone was tested for binding to the biotinylated spike protein domains, in order to assess specific
642 binding to the spike protein.
643
644 *Cloning of multivalent DARPin molecules*
645 Multivalent DARPin molecules were prepared using Gibson assembly as described(*50*). The individual
646 domains are linked with proline-threonine-rich polypeptide linkers(*50*) flanked by glycine-serine, with
647 a length of 24 amino acids (GSPTPTPTTPTPTPTTPTPTPTGS).
648
649 *DAPRin protein production and characterization*
650 DARPin molecules were expressed in *E. coli* and purified as described(*50*). Characterization of
651 monovalent DARPin molecules included SDS-PAGE, size exclusion chromatography, surface plasmon
652 resonance, SARS-CoV-2 pseudotype virus inhibition assay, as well as live virus inhibition assay.
653 Characterization of multivalent DARPin molecules included SDS-PAGE (fully intact size without
654 degradation; not shown), mass spectrometry (expected molecular weight; not shown), size exclusion
655 chromatography coupled to static light scattering, circular dichroism, storage stability (stable at 60°C
656 for 1 week; data not shown), serum stability (stable at 37°C in serum for one week; data not shown),
657 surface plasmon resonance, SARS-CoV-2 pseudotype virus inhibition assay, live virus inhibition assay,
658 hamster pharmacokinetic analysis, and hamster efficacy model as further described below.
659

660 *Circular dichroism of DARPin molecules*

661 Circular dichroism measurement was performed with a Jasco J-815 using a 1 cm pathlength cuvette
662 (Hellma) with the monitor sensor inserted in the cuvette. The MRE at 222 nm was followed over a
663 temperature ramp from 20°C to 90°C (heating and cooling). Spectra from 190-250 nm were taken
664 before and after the variable temperature measurement at 20°C. The protein was measured at
665 0.25 μM in PBS.

666

667 *Surface plasmon resonance affinity determination of DARPin molecules*

668 SPR assays were used to determine the binding affinity of monovalent DARPin as well as multivalent
669 DARPin molecules to the spike protein of SARS-CoV-2. All SPR data were generated using a Bio-Rad
670 ProteOn XPR36 instrument with PBS-T (0.005% Tween20) as running buffer. A new neutravidin sensor
671 chip (NLC) was air-initialized and conditioned according to Bio-Rad manual.

672 Monovalent DARPin molecules: Chemically biotinylated (via lysines) SARS-CoV-2 spike protein 20 (Sino
673 Biologics) was captured to ~3400 RUs (30 µg/ml, 30 µl/min, 300 s). Two buffer injections (100 µl/min,
674 60 s) followed by two 12.5 mM NaOH regeneration steps (100 µl/min, 18 s) were applied before the
675 first injections. Mono-domain DARPin proteins were injected (at 50/16.7/5.6/1.9/0.6 nM) for 180 s at
676 100 µl/min for association and dissociation was recorded for 3600 s (at 100 µl/min). The ligand was
677 regenerated with a 12.5 mM NaOH pulse (100 µl/min, 18 s). The data was double referenced against
678 the empty surface and a buffer injection and fitted according to the 1:1 Langmuir model.

679 Multivalent DARPin molecules: Chemically biotinylated (via lysines) COVID-19_S_protein_RBD_Fc
680 (Acro Biosystems) was captured to ~1000 RUs (775 ng/ml, 30 µl/min, 300 s). Two buffer injections
681 (100 µl/min, 60s) followed by two 12.5 mM NaOH regeneration steps (100 µl/min, 18s) were applied
682 before the first injections. One single concentration of 25 nM of each multi- domain drug candidate
683 was injected for 180 s at 100 µl/min for association and dissociation was recorded for 36'000 s (at
684 100 µl/min). The data was double referenced against the empty surface and a buffer injection. Due to
685 avidity gain, no significant dissociation could be recorded during the measured time.

686

687 *Cells and viruses*

688 Vero E6 cells (African green monkey kidney cells, ATCC® CRL1586™) purchased from ATCC (Manassas,
689 VA 20110 USA) were passaged in cell culture medium DMEM (FG0445) containing 10% FBS and
690 supplements (2mM L-Glutamine, Non-essential amino acids and 100 U/ml Penicillin 100 µg/ml
691 Streptomycin and HEPES, all from Biochrom, Berlin, Germany) at 37°C with CO2. SARS-CoV-2 (2019-
692 nCoV/IDF0372/2020) kindly provided by Dr. Sylvie van der Werf from the National Reference Centre

693 for Respiratory Viruses hosted by Institut Pasteur (Paris, France) was propagated in Vero E6 cells in
694 MEM containing 2% FBS and supplements (2%-FBS-MEM) at 37°C and 5% CO_2.
695 Virus neutralization capacity of monovalent DARPin and multivalent DARPin molecules was
696 determined for 100 $TCID_{50}$ SARS-CoV-2 by crystal violet staining of protected cells. DARPin molecules
697 were serially diluted from 50 nM to 3.2 pM (in triplicates) in 100 µl cell culture medium (2%-FBS-MEM)
698 enriched with 10 µM human serum albumin (HSA, CSL Behring, Switzerland) (2%-FBS-MEM + HSA) in
699 96 well plates. The diluted DARPin candidates were exposed to 100 $TCID_{50}$ SARS-CoV-2 (10^4 $TCID_{50}$/ml)
700 in 100 µl 2%-FBS-MEM + HSA. DARPin/virus mixtures (200 µl) were transferred onto 80% confluent
701 Vero E6 cells. The controls consisted of Vero E6 cells exposed to DARPin molecules only, to determine
702 unspecific effects of the DARPin molecules, of cells exposed to virus suspension only to determine
703 maximal cytopathic effect and of cells incubated with medium only, to determine baseline state of
704 cells. The plates were incubated for 3 days at 37°C and the cytopathic effect determined by staining
705 with 100 µl/well crystal violet solution (spatula tip (~4 mg) crystal violet powder (Sigma Aldrich) solved
706 in 30 ml 37% formalin and 120 ml PBS (Sigma Aldrich)) for 10 min and washing plates with PBS (Sigma
707 Aldrich). Wells were visually evaluated for complete protection indicated by intact blue/violet cell
708 layer or partial protection in case of >50% intact cell layer.
709 The effect of neutralization capacity of Multivalent DARPin was evaluated by exposing serial dilutions
710 of the DARPin candidates to increasing titers of SARS-CoV-2 and determining cell protection by
711 CellTiter-Glo assay (Promega, Madison, USA). Serial dilution of DARPin candidates were prepared in
712 96 well plates in 100 µl cell culture medium (2%-FBS-MEM + HSA) mixed with 100 µl virus suspension
713 of 10^4 $TCID_{50}$/ml SARS-CoV-2 and incubated for 1 h at 37°C and 5% CO_2. DARPin/virus mixtures (200
714 µl) were transferred onto 80% confluent Vero E6 cells and plates incubated at 37°C for 3 days. Cell
715 viability was determined by removing 100 µl supernatant from all wells and adding 100 µl CellTiter-
716 Glo reagent as described in the manufacturers protocol (CellTiter-Glo® Luminescent Cell Viability
717 Assay). Luminescence was read after 2 minutes shaking on an orbital shaker and 10 min incubation at
718 RT using the GloMax instrument (Promega, Madison, USA).
719
720 *SARS-CoV-2 VSV pseudotype virus assay*
721 SARS-CoV-2 pseudoviruses were generated as described previously(*51*). A selected panel of 380
722 DARPin molecules expressed in 96-well format and purified to homogeneity were evaluated for their
723 anti-viral activity in a pseudovirus screening assay. In parallel, 6 monovalent DARPin molecules of
724 known spike domain specificity which were randomly assembled in a set of 192 tri-specific DARPin
725 molecules were included in the screen. For the pseudovirus screening assays, DARPin molecules were
726 diluted in Dulbecco modified Eagle medium (DMEM)-2 % [vol/vol] fetal calf serum (FCS) at the

727 following concentrations: 200 nM, 20 nM, 2nM and 0.2 nM and mixed with an equal volume of DMEM-
728 2 % [vol/vol] FCS containing the VSV-based SARS-CoV-2 pseudoviruses to obtain 2000 IU/well. The mix
729 was incubated for 60 min at 37°C, then inoculated onto Vero E6 cells in a clear bottom white walled
730 96-well plate during 90 min at 37°C. The inoculum was removed and fresh medium added, and cells
731 further incubated at 37°C for 16 h. Cell were lysed according to the ONE-Glo™ luciferase assay system
732 (Promega, Madison, US) and light emission was recorded using a Berthold® TriStar LB941
733 luminometer. For the pseudovirus titrations an initial dilution of the drug was followed by two-fold
734 dilutions in quadruplicates in DMEM)-2 % [vol/vol] FCS supplemented with 20 µM human serum
735 albumin (CSL Behring). The mixture was mixed with an equal volume of DMEM-2 % FCS containing
736 SARS-CoV-2 pseudoviruses and incubated for 90 min at 37°C. Neutralizations were performed from
737 200 to 2000 infectious units (IU) per well, depending on the experiment. Following this incubation,
738 the mix was inoculated onto Vero E6 cells in a clear bottom white walled 96-well plate during 90 min
739 at 37°C. The inoculum was removed and fresh medium added, and cells further incubated at 37°C for
740 16 h. Cell were lysed according to the ONE-Glo™ luciferase assay system (Promega, Madison, US) and
741 light emission was recorded using a Berthold® TriStar LB941 luminometer. The raw data (relative light
742 unit values) were exported to GraphPad Prism v8.01, and the % neutralization data were normalized
743 to the untreated PsV signal. IC_{50} with 95% confidence interval were estimated by model of nonlinear
744 regression fit with settings for log (inhibitor) vs normalized response curves.
745 Laboratory 2: PsV NA for titration curves
746 Production of VSV pseudotyped with SARS2-S was described previously(*52*). Briefly, HEK-293T cells
747 were transfected with pCAGGS expression vectors encoding MERS-S, SARS-S or SARS2-S carrying a 16-
748 , 28- or 18-a.a. cytoplasmic tail truncation, respectively. One day post transfection, cells were infected
749 with the VSV-G pseudotyped VSVΔG bearing the firefly (Photinus pyralis) luciferase reporter gene.
750 Twenty-four hours later, supernatants containing SARS2-S pseudotyped VSV particles were harvested
751 and titrated on African green monkey kidney Vero E6 (ATCC#CRL-1586) cells.
752 In the virus neutralization assay, DARPin molecules were threefold serially diluted at two times the
753 desired final concentration in DMEM supplemented with 10 µM human serum albumin (CSL Behring),
754 100 U/ml Penicillin and 100 µg/ml Streptomycin (Lonza). Monoclonal antibodies against MERS-S (2),
755 SARS-S or SARS2-S were included as a positive control(*52*). Diluted DARPin molecules and mAbs were
756 incubated with an equal volume of pseudotyped VSV particles for 1 hour at room temperature,
757 inoculated on confluent Vero E6 monolayers in 96-well plate, and further incubated at 37 °C for
758 24 hours. Cells were lysed with Luciferase Cell Culture Lysis 5X Reagent (Promega) at room
759 temperature for 30 min. Luciferase activity was measured on a Berthold Centro LB 960 plate

760 luminometer using D-luciferin as a substrate (Promega). The half maximal inhibitory concentrations
761 (IC_{50}) were determined using 4-parameter logistic regression (GraphPad Prism version 8).
762
763 *Cryo-electron microscopy*
764 4 µl of purified S ectodomain (9 µM) was mixed with 1 µl of 50 µM mono-DAPRin #3, #9 or #10, and
765 incubated for 15 seconds at room temperature. 3 µl of sample was then dispensed on Quantifoil
766 R1.2/1.3 200-mesh grids (Quantifoil Micro Tools GmbH) that had been freshly glow discharged for 30 s
767 at 20 mA. Grids were blotted using blot force +2, for 5 s using Whatman No. 1 filter paper and
768 immediately plunge-frozen into liquid ethane cooled by liquid nitrogen using a Vitrobot Mark IV
769 plunger (Thermo Fisher Scientific) equilibrated to ~95% relative humidity, 4°C. Movies of frozen-
770 hydrated specimens were collected using Glacios Cryo-TEM (Thermo Fisher Scientific) operating at
771 200 keV and equipped with a Falcon 4 Direct Electron Detector (Thermo Fisher Scientific). For
772 additional analysis of monovalent DARPin #3, 4 µl of purified S ectodomain (18 µM) was mixed with 1
773 µl of 100 µM DARPin, and incubated for 60 s at room temperature. Grids were prepared as described
774 above, and movies were collected using a Titan Krios Cryo-TEM (Thermo Fisher Scientific) operating
775 at 300 keV and equipped with a Falcon 4 Direct Electron Detector (Thermo Fisher Scientific). All cryo-
776 EM data were acquired using the EPU 2 software (Thermo Fisher Scientific) with a 30-degree stage tilt
777 to account for preferred orientation of the samples. Movies were collected in electron counting mode
778 at 92,000x (Glacios) or 75,000x (Titan Krios), corresponding to a pixel size of 1.1 Å/pix or 1.045 Å/pix
779 over a defocus range of -1.25 to -2.5 µm.
780
781 *Image processing*
782 Movie stacks were manually inspected and then imported in Relion version 3.1(*53*). Drift and gain
783 correction were performed with MotionCor2(*54*), and GCTF(*55*) was used to estimate the contrast
784 transfer function for each movie. Particles were automatically picked using the Laplacian-of-Gaussian
785 (LoG) algorithm and then Fourier binned (2 x 2) particles were extracted in a 160-pixel box. The
786 extracted particles were subjected to two rounds of 2D classification, ignoring CTFs until the first peak.
787 Using the 'molmap' command in UCSF chimera(*56*), a SARS-CoV-2 spike structure (PDB ID: 6VSB)(*23*)
788 was used to generate a 50 Å resolution starting model for 3D classification. Particles selected from 2D
789 classification were subject to a single round of 3D classification (with C1 symmetry). Particles
790 belonging to the best classes were re-extracted unbinned in a 320-pixel box, 3D auto-refined (with C1
791 or C3 symmetry) and post-processed. Iterative rounds of per particle defocus estimation, 3D auto-
792 refinement and post-processing were used to account for the 30-degree stage tilt used during data
793 collection. When CTF refinement did not yield any further improvement in resolution, Relion's

794 Bayesian polishing procedure was performed on the particle stacks, with all movie frames included,
795 followed by 3D auto-refinement and post-processing. Subsequently, additional rounds of per particle
796 defocus estimation, 3D auto-refinement and post-processing were performed on the polished
797 particles until no further improvement in resolution or map quality was observed. The nominal
798 resolution for each map was determined according to the 'gold standard' Fourier shell correlation
799 (FSC) criterion (FSC = 0.143) and local resolution estimations were performed using Relion. Map
800 sharpening was performed using DeepEMhancer(*57*) as implemented in COSMIC2(*58*). To improve
801 the quality of the mono-DARPin #3 density in the fully open spike reconstruction, a focused 3D
802 classification approach was employed. Briefly, each particle contributing to the final C3-symmetry–
803 imposed reconstruction was assigned three orientations corresponding to its symmetry related views
804 using the "relion_particle_symmetry_expand" tool. A soft mask was placed over the map to isolate
805 the mono-DARPin #3-bound RBD, and the symmetry-expanded particles were subjected to masked
806 3D classification without alignment using a regularization parameter ('T' number) of 20. Particles
807 corresponding to the 3D class with the best resolved DARPin density were re-extracted in a 200-pixel
808 box and centered on the mask used for focused classification. In conjunction with this, the signal for
809 the protein outside the masked was subtracted. The re-extracted particles were then 3D auto-refined
810 (with C1 symmetry) using local angular searches (1.8 degrees) and sharpened using
811 DeepEMhancer(*57*). Three copies of the locally refined map were aligned to the globally refined map
812 using the UCSF Chimera 'fit in map' tool and resampled using the 'vop resample' command. Finally, a
813 composite map was generated using the "vop add" command. An overview of the image processing
814 workflows for each of the monovalent DARPin samples is shown in supplementary Figure 2.
815
816 *Molecular modeling of mono and multivalent DARPin molecules*
817 Homology models of monovalent DARPin molecules #3 and #9 were generated with Rosetta(*59*). The
818 consensus designed ankyrin repeat domain PDB ID:2xee was used as template. Mutations were
819 introduced with RosettaRemodel(*60*) with fixed backbone, and the structure was refined with
820 RosettaRelax(*61*). Forty refined structures were clustered using RosettaCluster with 0.3 Å radius, and
821 the lowest-energy model from the largest cluster served as the final model. These models were then
822 used for fitting domain #3 and #9 into the observed electron density generated from the complex
823 structure of the spike protein.
824 To facilitate accurate fitting of the DARPin coordinates into their respective cryo-EM maps, difference
825 density maps of the bound DARPin molecules were produced as described previously(*62*). For
826 monovalent DARPin #3, the atomic coordinates of a fully-open spike ectodomain (PDB ID: 6XCN) were
827 fitted into the EM density using the UCSF Chimera 'fit in map' tool. The Fab component of the model

828 was deleted, and then the 'molmap' command was used to simulate a 7 Å resolution density map.
829 This simulated map was then resampled on the grid of the experimental cryo-EM density map using
830 the 'vop resample' command. The 'vop subtract' command was then used to subtract the value of the
831 simulated map from the experimental map. The 'minRMS' option was used to automatically scale the
832 simulated map to minimize the root-mean-square sum of the resulting subtracted values at grid points
833 within the lowest contour of simulated map. The UCSF Chimera 'fit in map' tool was then used to fit
834 monovalent DARPin #3 into the difference density until the correlation between the map and model
835 did not improve any further, and ensuring that the epitope binding surface of the monovalent DARPin
836 was orientated towards the spike ectodomain. This workflow was then repeated for monovalent
837 DARPin #9, using the fully closed spike coordinates (PDB ID: 6ZGE).
838
839 The PDB file with the coordinates of the trimer of domain #3:RBD was used as an input structure for
840 the conceptual modeling of MR-DC bound to the spike ectodomain as shown in Supplementary Figure
841 8. In both models, the open RBD domain from PDB ID 6vyb was used to generate three RBDs in the
842 open conformation(*13*). For the conceptual modeling of MM-DC a similar approach was used by fitting
843 domain #9 into the observed density of the NTD cryo-EM structure. Additionally, a structurally
844 resolved NTD domain from PDB 7c2l was used(*26*), and a binding domain model of S2 (#10) was placed
845 manually to a potential interacting site on S2 (non-glycosylated region within reasonable distance
846 from the binding domain #9, based on linker length). For both structures, HSA binding DARPin models
847 were placed and the linkers between each binding domain were modeled using Rosetta modeling
848 tools(*60*).
849
850 In a last step, the models of monovalent DARPin #3:RBD (residues 303-526) and monovalent DARPin
851 #9:NTD (residues 14-303) were refined with Rosetta. The structures were pre-relaxed for docking and
852 served as input for local, high-resolution docking with RosettaDock(*63*) with fixed backbone. Five
853 hundred models were generated and clustered with 1 Å radius (RosettaCluster). Two largest clusters
854 were inspected and the lowest-energy model from more conserved group (i.e., with lower rigid-body
855 perturbation from the input structure) was taken further for additional all-atom refinement with
856 RosettaRelax(*61*), with protocol optimized for interfaces (InterfaceRelax2019). Fifty models were
857 generated, and the lowest scoring model was selected. This model was used to describe the
858 interactions between DARPin molecules and their target domains. Figures were generated using
859 LigPlot(*64*), UCSF Chimera(*56*), UCSF ChimeraX(*65, 66*), PyMOL (The PyMOL Molecular Graphics
860 System, Version 2.0, Schrödinger, LLC) and BioRender (BioRender.com).

861 *Prophylactic Syrian golden hamster model for the assessment of antiviral potency of candidate MR-DC*
862 *The study was performed at Viroclinics Xplore, Schaijk, The Netherlands.*
863 *Virus used for Syrian golden hamster study*
864 SARS-CoV-2 isolate BetaCoV/Munich/BavPat1/2020 was kindly provided by Prof. Dr. C. Drosten
865 (European Virus Archive Global # 026V-03883). With a history of 1 passage in Vero-TMPRSS2 and 3
866 passages in Vero E6 cells (ATCC), the seed stock was titrated in Vero E6 cells to a concentration of 7.1
867 log10 $TCID_{50}$/ml. The seed stock was thawed and diluted in cold phosphate-buffered saline (PBS) prior
868 to infection.
869 *Experimental design*
870 Twenty-four specific-pathogen-free (SPF) 15 weeks-old Syrian golden hamsters (Mesocricetus
871 auratus, females and males, approximate body weights of 160g, provided by Envigo) were uniquely
872 identified using individually-coded animal markers. They were housed in elongated type 2 group cages
873 with two animals per cage under BSL-III conditions during the experiment. They were kept according
874 to the standards of Dutch law for animal experimentation and were checked daily for overt signs of
875 disease. The study was carried out following approval by an independent animal welfare body
876 (approval AVD277002015283-WP13) and complied with all relevant ethical regulations for animal
877 testing.
878 Four groups of six hamsters were treated with multivalent DARPin molecule MR-DC via the
879 intraperitoneal route with 16 µg, 160 µg, or 1600 µg doses per animal or with a placebo 24 hours prior
880 to infection and subsequently animals were inoculated intra-nasally with 100 µL PBS containing
881 $5x10^4$ $TCID_{50}$ SARS-CoV-2. The inoculum was instilled dropwise using a pipette and equally divided over
882 both nostrils. The animals were weighed regularly and throat swabs, for quantitative PCR and
883 infectious virus titration, were collected on a daily basis. For all animal procedures, the animals were
884 sedated with isoflurane (3-4%/O2).
885 Upon necropsy at day 4 post infection, full-body gross pathology was performed for each animal and
886 all abnormalities recorded and described. All lung lobes were inspected, and the percentage of
887 affected lung tissue was estimated by eye. Samples of the left nasal turbinates, trachea and the entire
888 left lung (often with presence of the primary bronchi) were preserved in 10% neutral buffered formalin
889 for histopathology. Samples of the right lung parenchyma and right nasal turbinates were frozen for
890 quantitative PCR and virus titration.
891 *Virology*
892 Throat swabs and homogenized tissue samples (lungs and nasal turbinates) were thawed and tested
893 for the presence of SARS-CoV-2 infectious virus using virus titration. To this end, quadruplicate 10-fold
894 serial dilutions were used to determine the virus titers on confluent layers of Vero E6 cells. Serial

895 dilutions of the samples (throat swabs and tissue homogenates) were prepared and incubated on Vero
896 E6 monolayers for 1 hour at 37°C. Vero E6 monolayers were washed and incubated with infection
897 medium for 4-6 days at 37°C after which plates were scored for cytopathogenic effect (CPE) using the
898 vitality marker WST-8. Viral titers ($TCID_{50}$) were calculated using the method of Spearman-Karber.
899 *Histopathology*
900 Samples of tissue from the respiratory tract (lung, trachea, and nasal turbinates) and lymphoid organs
901 (spleen and mandibular lymph node) were fixed in 10% neutral buffered formalin (24-48h) and
902 embedded in paraffin. Tissue sections were then stained with hematoxylin and eosin and examined
903 by light microscopy. A semi-quantitative histopathological analysis was performed, and findings
904 scored using the following grades: absent (grade 0), minimal (grade 1), mild (grade 2), moderate
905 (grade 3) or marked (grade 4). The average score for the dose groups was calculated for each finding
906 in the respiratory tract (Figure 4b) and lymphoid organs (Figure 4c).
907
908 *Hamster pharmacokinetic study*
909 Single-dose intraperitoneally administered dose pharmacokinetic measurements in female hamsters
910 (n = 6 per group) were performed at 1 mg/kg and 10 mg/kg. Blood samples were collected pre-dose
911 and again at 1 h, 4 h, 8h, 12h, 24 h, 48 h, 72 h, 96 h and 168 h post-injection. Serum concentrations
912 were determined by sandwich ELISA using RBD as capture reagent and an anti-His-tag antibody as
913 detection reagent and using a standard curve. Pharmacokinetic parameters were determined using
914 the software Phoenix WinNonLin (Certara, Princeton, USA) or GraphPadPrism (GraphPad Software, La
915 Jolla,USA) and non-compartmental analyses.
916

917 **Supplementary Figures**

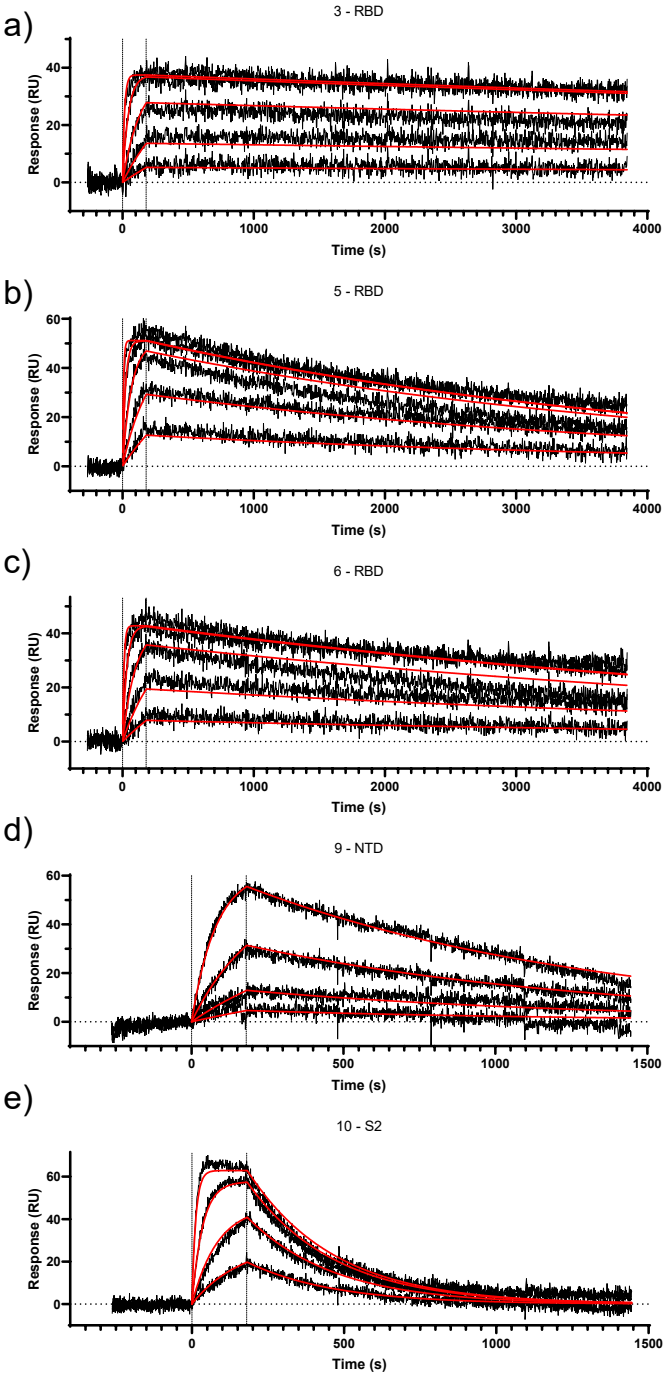

918

919

920

921

922

923 **Supplementary Figure 1**: Surface plasmon resonance (SPR) sensorgrams of the monovalent DARPin

924 molecules #3 (a), #5 (b), #6 (c), #9 (d), #10 (e), incorporated in MR-DC (a-c) and MM-DC (c-e) binding

925 to immobilized trimeric spike protein. DARPin concentrations for a-c: 50/16.67/5.56/1.85/0.62 nM.

926 DARPin concentrations for (d) and (e): 16.67/5.56/1.85/0.62 nM. Affinity values of monovalent

927 DARPin molecules are listed in **Table 1**.

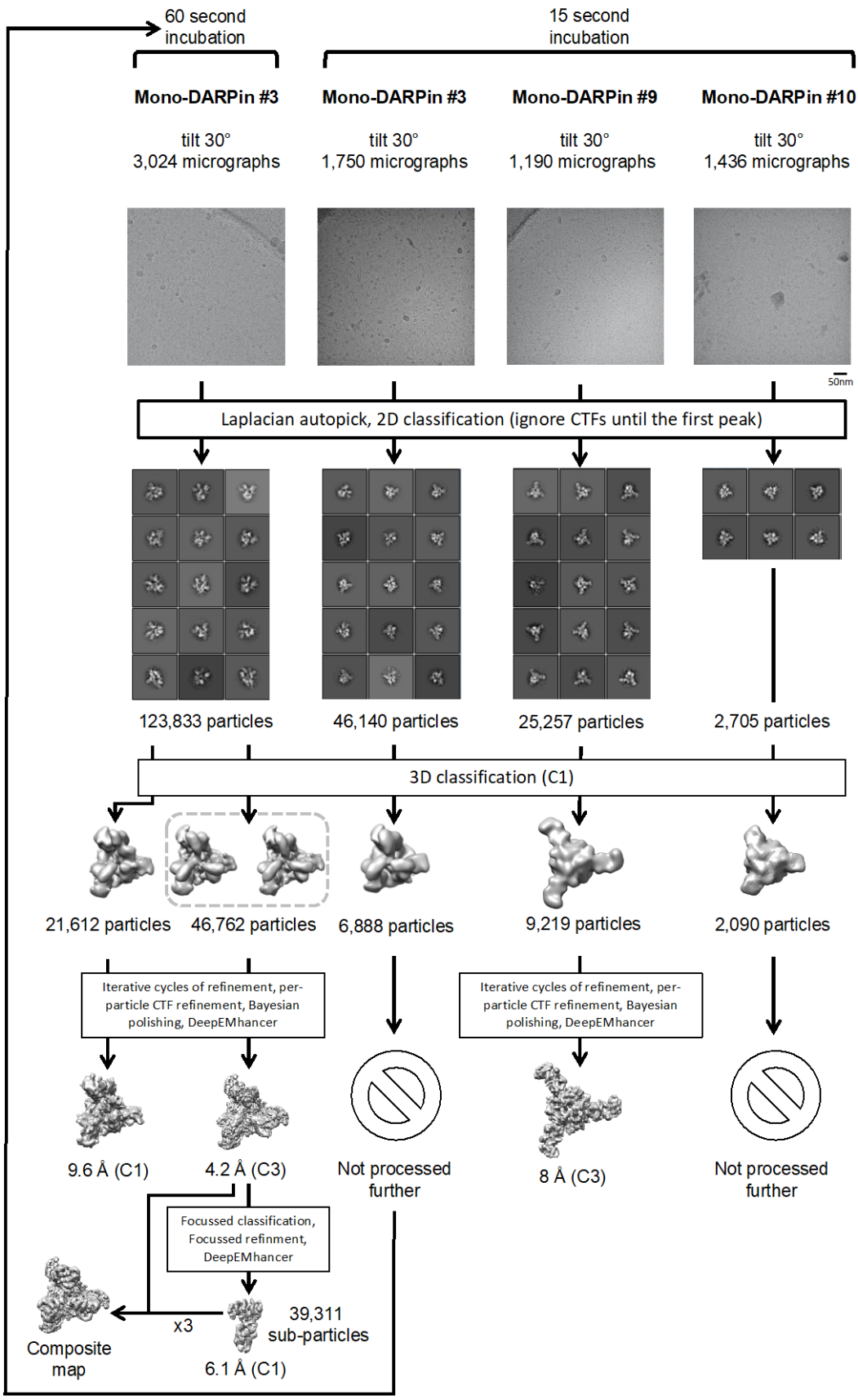

Supplementary Figure 2: Single-particle cryo-EM image processing workflows for each of the monovalent DARPin samples.

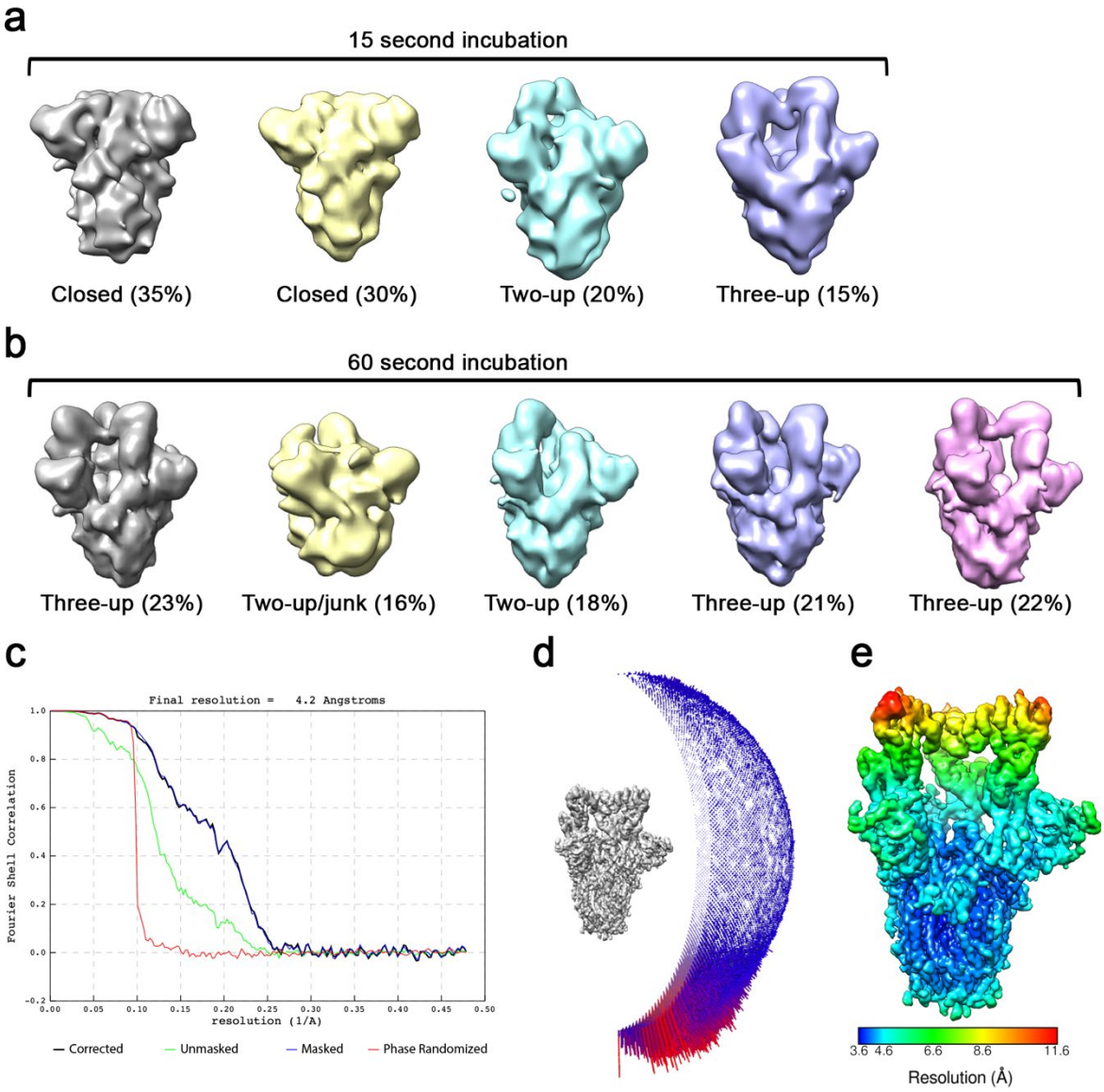

Supplementary Figure 3: a) 3D classes obtained from spike ectodomains incubated with monovalent DARPin #3 for 15 seconds, and b) for 60 seconds. c) Gold-standard Fourier shell correlation (FSC) curve generated from the independent half maps contributing to the 4.2 Å resolution density map. d) Angular distribution plot of the final C3 refined EM density map. e) The EM density map of the spike ectodomain bound to three copies of monovalent DARPin #3, colored according to local resolution.

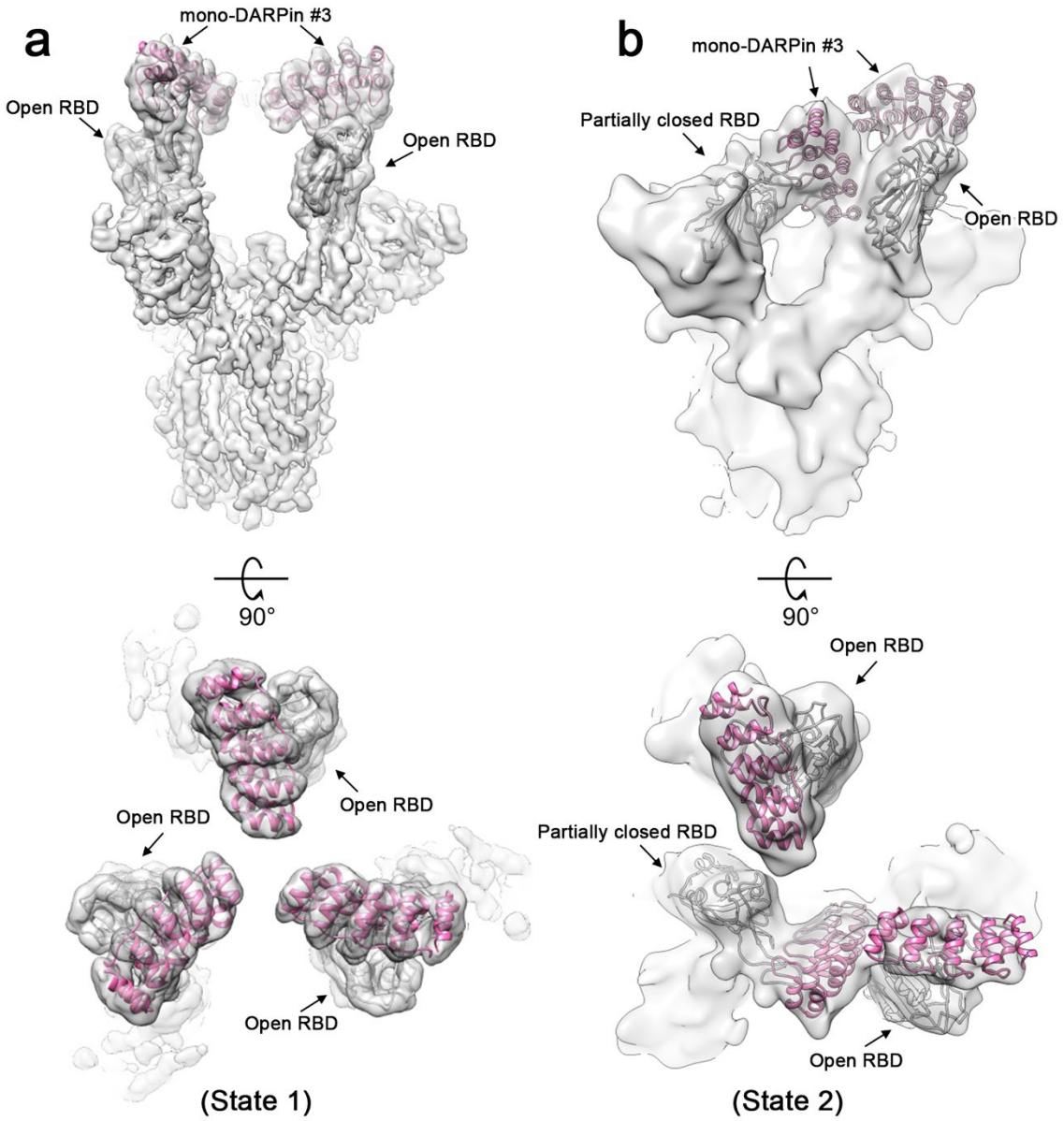

Supplementary Figure 4: a) Cryo-EM density for state 1 and b) state 2 of the SARS-CoV-2 spike ectodomain in complex with the RBD targeting monovalent DARPin #3, shown as two orthogonal views. The pseudo-atomic model of monovalent DARPin #3 in complex with RBD, derived from molecular docking experiments, is fitted in each of the spike protomers and colored grey and pink, respectively.

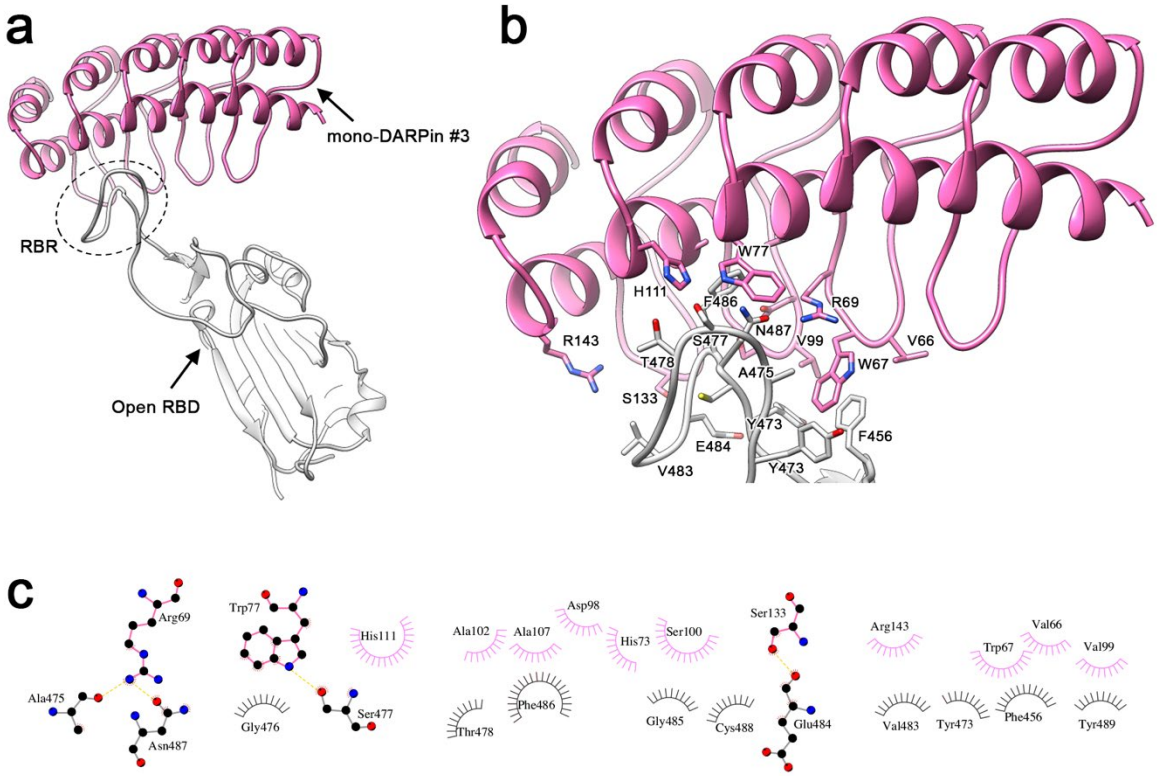

Supplementary Figure 5: a) Pseudo-atomic model of monovalent DARPin #3 in complex with the SARS-COV-2 spike RBD colored grey and pink, respectively. b) Zoomed in view of the interface between monovalent DARPin #3 and RBD. c) DimPlot(*67*) representation of putative interacting residues between the spike ectodomain RBD and monovalent DARPin #3, identified through molecular docking experiments. Residues participating in hydrophobic interactions are shown as spoke arcs. Residues participating in hydrogen bonding are shown as sticks, and hydrogen bonds are shown as yellow dotted lines. Residues are coloured grey and pink for spike and monoDARPin #3, respectively.

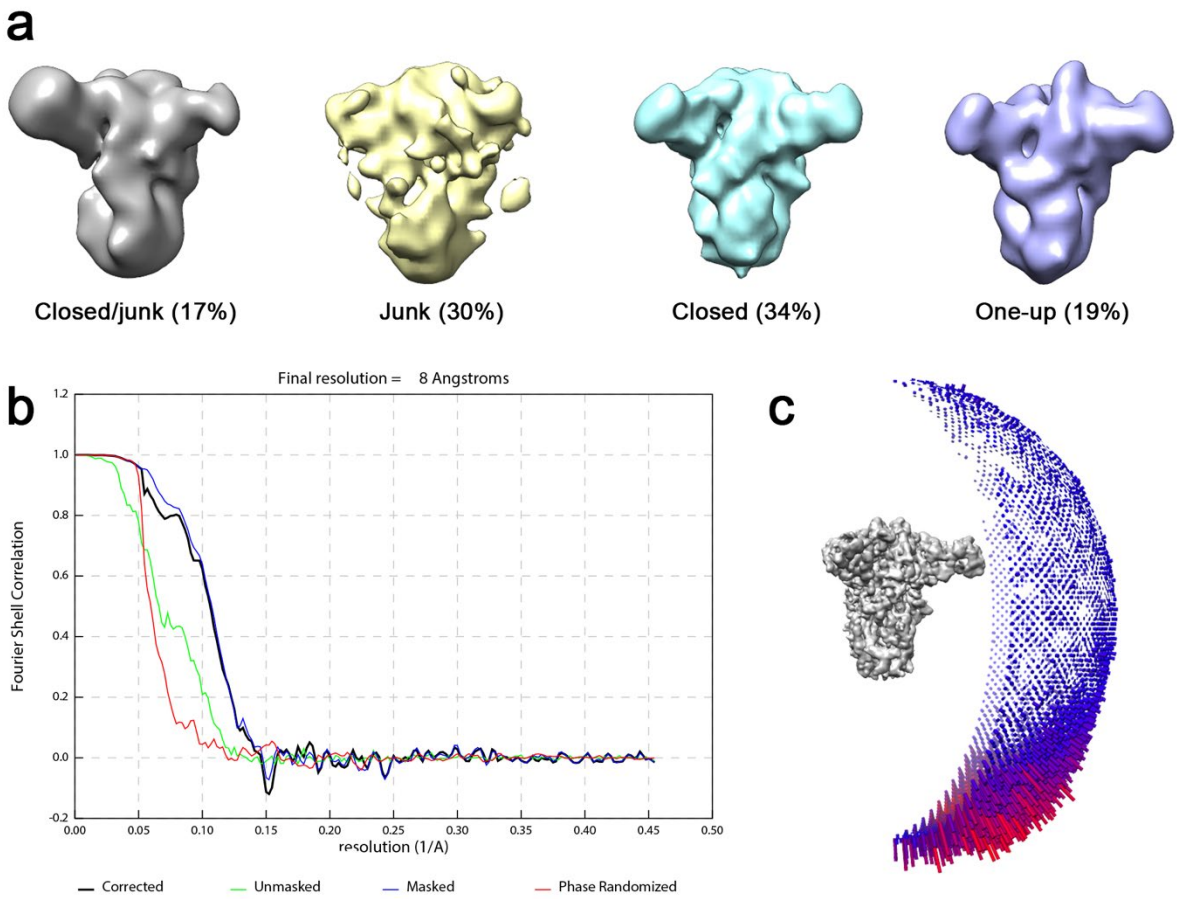

Supplementary Figure 6 a) 3D classes obtained from spike ectodomains incubated with monovalent DARPin #9 for 15 seconds. b) Gold-standard Fourier shell correlation (FSC) curve generated from the independent half maps contributing to the 8 Å resolution density map. c) Angular distribution plot of the final C3 refined EM density map.

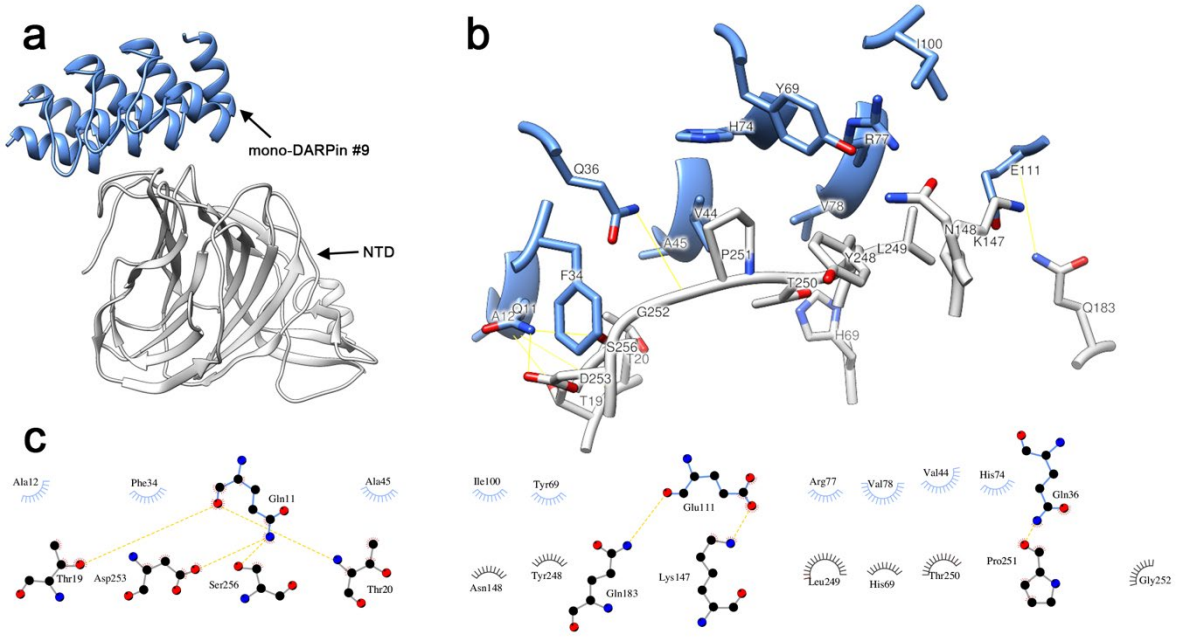

Supplementary Figure 7: a) Pseudo-atomic model of monovalent DARPin #9 in complex with the SARS-COV-2 spike NTD colored blue and grey, respectively. b) Zoomed in view of the interface between monovalent DARPin #9 and NTD. c) DimPlot(*67*) representation of putative interacting residues between the spike ectodomain NTD and monovalent DARPin #9, identified through molecular docking experiments. Residues participating in hydrophobic interactions are shown as spoke arcs. Residues participating in hydrogen bonding are shown as sticks, and hydrogen bonds are shown as yellow dotted lines. Residues are coloured grey and blue for spike and monovalent DARPin #9, respectively.

968

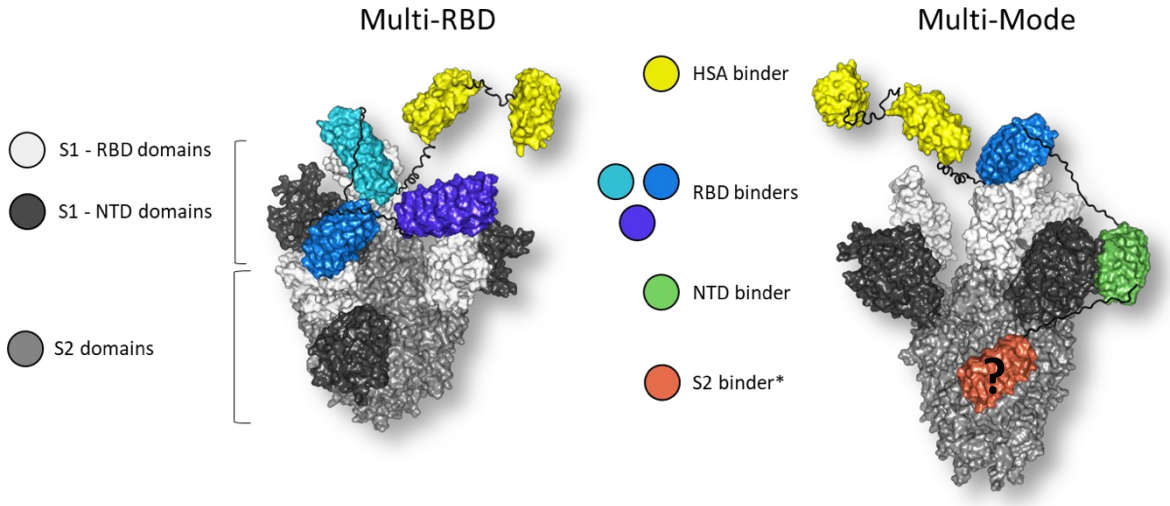

969

970 **Supplementary Figure 8:** Molecular model of multivalent DARPin molecule MM-DC (right), consisting
971 of five DARPin domains (yellow: HSA-binding domains, blue: RBD-binding domain, green: NTD-binding
972 domain, orange: S2-binding domain) bound to the spike ectodomain. Linkers are shown in black.
973 Molecular model of MR-DC (left) consisting of five DARPin domains (yellow: HSA-binding domains,
974 shades of blue: RBD-binding domains) bound to the RBDs (white) of the spike ectodomain (grey).
975 Linkers are shown in black. Position of RBD and NTD binders guided by Cryo-EM data (Figure 3) - *For
976 the S2 binder, the epitope is unknown.

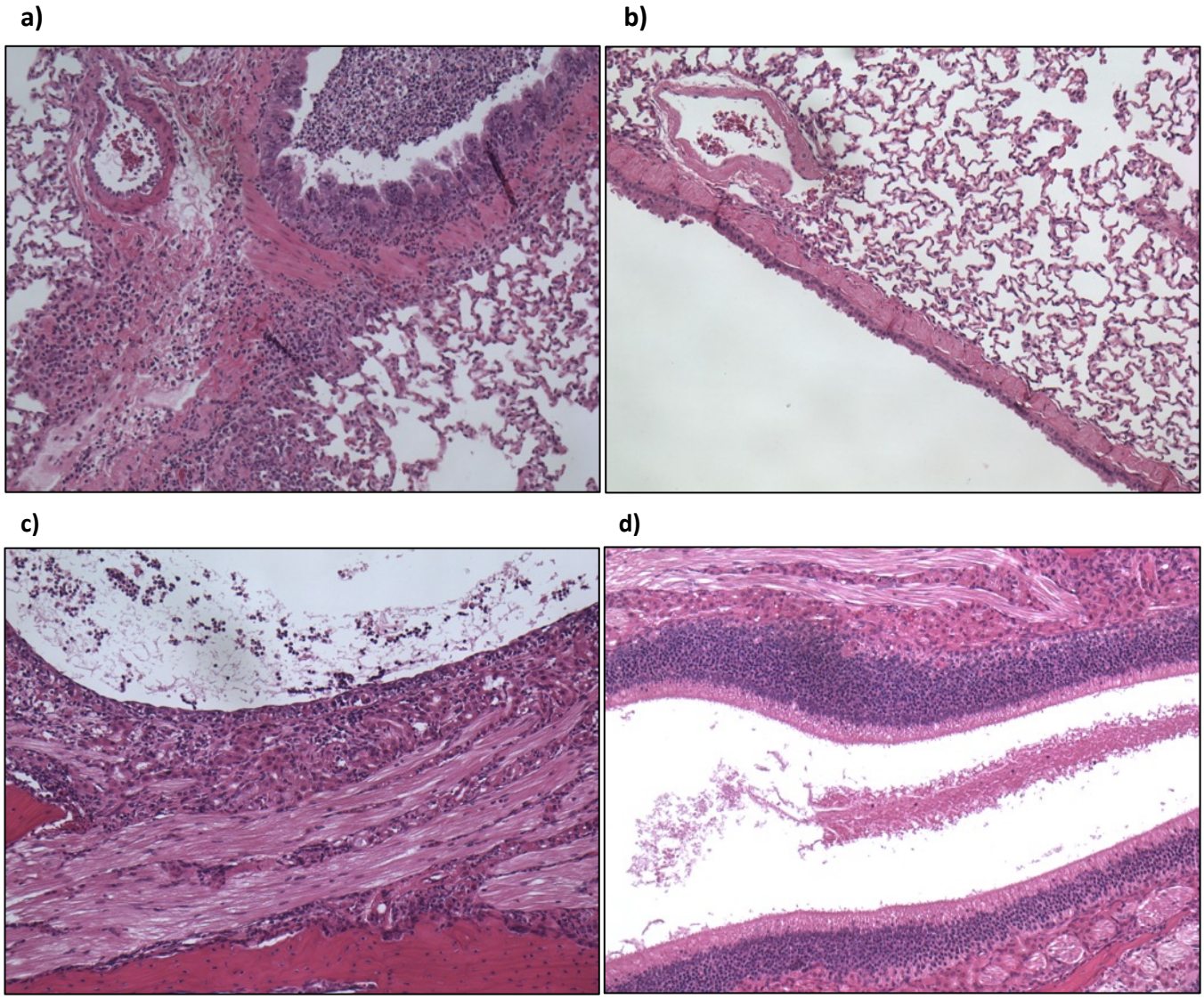

Supplementary Figure 9: Representative histopathological microscopic images of lung and nasal turbinates on day 4.

a) Lung from a hamster treated with vehicle: Moderate mixed inflammatory cell infiltrate (lymphocytes, macrophages, plasma, cells and granulocytes) of the bronchial/bronchiolar epithelium and underlying lamina propria extending to the adjacent blood vessels, alveolar interstitium and spaces with prominent Type II alveolar pneumocytes. Some degeneration, regeneration and disorganization of the bronchial epithelium with single cell necrosis is also evident. b) Lung from a hamster treated with 1600 ug: Very minimal mixed inflammatory cell infiltrate (lymphocytes, macrophages, plasma, cells and granulocytes) of the bronchial/bronchiolar epithelium and underlying lamina propria. c) Nasal turbinates from a hamster treated with vehicle: A marked mixed inflammatory cell infiltrate (lymphocytes, macrophages, plasma, cells and granulocytes) of the olfactory epithelium with degeneration, regeneration and disorganization of the epithelium, single cell necrosis and inflammatory exudate in the lumen of the nasal cavity. d) Nasal turbinates from a hamster treated

1010 with 1600 ug: A mild mixed inflammatory cell infiltrate (lymphocytes, macrophages, plasma, cells and
1011 granulocytes) of the olfactory epithelium with degeneration, regeneration and disorganization of the
1012 epithelium, single cell necrosis and inflammatory exudate in the nasal cavity.
1013

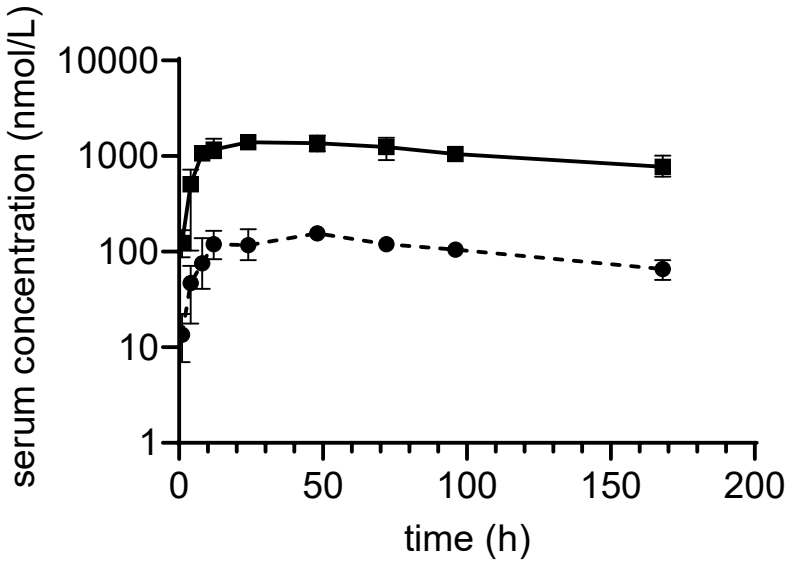

1014

1015 **Supplementary Figure 10:** Pharmacokinetic analysis of MR-DC exposure at concentrations of 1 mg/kg
1016 (dashed line) and 10 mg/kg (solid line), following i.p. administration. Elimination half-life was
1017 calculated to be 4-6 days.

1018 # Supplementary Tables

1019 **Supplementary Table 1**: List of spike protein-binding monovalent DARPin molecules and their
1020 properties

Name		*Binding domain*	*Viral Neutralization*	*PsV NA – Screening** [nM]	*K_D [nM]*	*SEC Profile*	*Tm [°C]*	*Size [kDa]*
1		RBD	Neutralizing	10	0.258**	Monomer	*>65*	*~14*
2		RBD	Neutralizing	10	0.220***	Monomer	>85	*~17*
3		RBD	Neutralizing	10	0.030**	Monomer	>85	*~17*
4		RBD	Neutralizing	10	0.390***	Monomer	>85	*~17*
5		RBD	Neutralizing	10	0.090**	Monomer	>85	*~17*
6		RBD	Neutralizing	10	0.080**	Monomer	>85	*~17*
7		RBD	Non-neutralizing	no neutralization	8.10***	Monomer	>80	*~14*
8		RBD	Non-neutralizing	no neutralization	10.0***	Monomer	n.a.	*~14*
9		NTD	Non-neutralizing	no neutralization	1.24**	Monomer	n.a.	*~14*
10		S2	Partial Neutralization	100	0.785**	Monomer	>85	*~14*
11		S2	Partial Neutralization	100	n.a.	Monomer	>85	*~17*

1021 ** VSV-SARS-CoV-2 pseudoviron screening assays were performed at 1, 10 and 100nM for all monovalent DARPin molecules. The value indicated*
1022 *is the lowest concentration where neutralization or partial neutralization was detected.*
1023 *** Multi concentration SPR measurement*
1024 **** Single concentration SPR measurement*
1025 *n.a.: not applicable*

1026 **Supplementary Table 2:** Properties of SARS-CoV-2 inhibiting DARPin candidates

Construct Name	5D-Multivalent DARPin					IC$_{50}$ PsV NA (*Screening Assay 1)	IC$_{50}$ PsV NA (*Screening Assay 2)	Live Virus CPE**	SEC Profile	Tm [°C] (CD)
	1	2	3	4	5	[10^{-9} M]	[10^{-9} M]	[10^{-9} M]		
MR-DC	**H**	**H**	**6**	**3**	**5**		**0.199**	**0.025**	**Monomeric**	**>85**
MM-DC	**H**	**H**	**5**	**9**	**10**	**0.228**		**0.100**	**Monomeric**	**>85**
M3	H	H	6	1	3	0.120		0.080	Monomeric	>80
M4	H	H	4	2	1		0.261	0.080	Monomeric	>75
M5	H	H	4	6	3		0.281	n.a	Monomeric	>85
M6	H	H	6	3	6	0.125		0.016	Monomeric	>85
M7	H	H	7	3	6	0.241		0.016	Monomeric	>80
M8	H	H	8	4	1	0.238		0.080	Monomeric	>85
M9	H	H	4	1	8	0.263		0.050	Monomeric	>85
M10	H	H	3	6	9	0.264		0.080	Monomeric	>85
M11	H	H	9	3	6	0.279		0.080	Monomeric	>80
M12	H	H	1	6	9	0.418		0.080	Monomeric	>75
M13	H	H	9	6	1	0.476		0.080	Monomeric	>80
M14	H	H	6	9	10	0.098		0.080	Monomeric	>80
M15	H	H	3	9	11	1.267		0.800	Monomeric	>85
M16	H	H	10	9	6	0.147		0.050	Monomeric	>85
M17	H	H	11	9	3	0.693		n.a	Monomeric	>80
M18	H	H	5	1	3		0.386	n.a	Monomeric	>80
M19	H	H	1	2	5		0.354	0.080	Monomeric	>80
M20	H	H	3	5	6		0.256	0.016	Monomeric	>85
M21	H	H	6	10	11		0.201	0.080	Monomeric	>85
M22	H	H	3	10	10		0.141	0.016	Monomeric	>80

H = Human serum albumin binding DARPin

n.a. = not applicable

** Higher viral titers used during the screening process compared to illustrated titration curves, which results in higher IC50 values*

*** Titration assays for evaluation of cytopathic effect (CPE) by crystal violet staining. Displayed is the lowest concentration where cell protection was observed.*

1027 **Supplementary Table 3**: Neutralization potency (IC_{50}, [pM]) for multivalent DARPin molecules MR-DC
1028 and MM-DC for SARS-CoV-2 spike protein variants, frequently observed in sequencing data of globally
1029 appearing serotypes, were evaluated by PsV NA.

	wt	G476S	V483A	D614G	D614G x Q675H
MR-DC	16.53	27.08	27.48	11.77	12.11
MM-DC	5.48	14.46	32.40	4.64	22.44

1030 **Supplementary Table 4:** Cryo-EM data collection and image processing information.

Monovalent DARPin (no.)	#3	#3	#3	#9	#10
Magnification	75,000	75,000	92,000	92,000	92,000
Voltage (kV)	300	300	200	200	200
Electron exposure (e-/Å^2)	40	40	40	40	40
Defocus range (μm)	1.25-2.5	1.25-2.5	1.25-2.5	1.25-2.5	1.25-2.5
Pixel size (Å)	1.045	1.045	1.1	1.1	1.1
Symmetry imposed	C3	C1	N/A	C3	N/A
Initial particle images (no.)	123,833	123,833	46,140	25,257	2,705
Final particle images (no.)	46,762	21,612	6,888	9,219	2,090
Map resolution (Å)	4.2	9.6	N/A	8	N/A
FSC threshold	0.143	0.143	N/A	0.143	N/A
Map resolution range (Å)	3.7-14.1	8.2-26	N/A	6.9-18.5	N/A

1031 **Supplementary Table 5:** Overview of fermentation runs performed with anti-SARS-Cov-2 multivalent
1032 DARPin molecule MP0420 at different scales. Expression yields presented in gram product per liter
1033 fermentation broth were determined by SDS-PAGE.

Run	Status	Fermenter Scale	Harvested Amount	Expression Yield
1	Development	5 L	4.9 kg	12.6 g/L
2	Development	5 L	4.9 kg	12.5 g/L
3	Development	5 L	4.9 kg	11.1 g/L
4	GMP	100 L	101 kg	11.3 g/L
5	GMP	100 L	101 kg	12.3 g/L

1034